

The Multipolar Magnetic Field of Millisecond Pulsar PSR J0030+0451

CONSTANTINOS KALAPOTHARAKOS  ^{1,2} ZORAWAR WADIASINGH  ^{2,3} ALICE K. HARDING  ² AND DEMOSTHENES KAZANAS  ²

¹ University of Maryland, College Park (UMCP/CRESST II)
College Park, MD 20742, USA

² Astrophysics Science Division, NASA/Goddard Space Flight Center
Greenbelt, MD 20771, USA

³ Universities Space Research Association (USRA)
Columbia, MD 21046, USA

ABSTRACT

Modeling of the *NICER* X-ray waveform of the pulsar PSR J0030+0451, aimed to constrain the neutron star mass and radius, has inferred surface hot-spots (the magnetic polar caps) that imply significantly non-dipolar magnetic fields. To this end, we investigate magnetic field configurations that comprise offset dipole plus quadrupole components using static vacuum field and force-free global magnetosphere models. Taking into account the compactness and observer angle values provided by Miller et al. (2019) and Riley et al. (2019), we compute geodesics from the observer plane to the polar caps to compute the resulting X-ray light curve. We explore, through Markov chain Monte Carlo techniques, the detailed magnetic field configurations that can reproduce the observed X-ray light curve and have discovered degeneracies, i.e., diverse field configurations, which can provide sufficient descriptions to the *NICER* X-ray waveforms. Having obtained the force-free field structures, we then compute the corresponding synchronous γ -ray light curves following Kalapotharakos et al. (2014); these we compare to those obtained by *Fermi-LAT*, to provide models consistent with both the X-ray and the γ -ray data, thereby restricting further the multipole field parameters. An essential aspect of this approach is the proper computation of the relative phase between the synchronous X- and γ -ray light curves. We conclude with a discussion of the broader implications of our study.

Keywords: Pulsars — Millisecond Pulsars — X-ray astronomy — Gamma-ray astronomy — Stellar magnetic fields — Markov chain Monte Carlo — General relativity — Space telescopes

1. INTRODUCTION

Rotation-powered pulsars are known to exhibit emission across the entire observed electromagnetic spectrum, from radio to TeV γ -rays. While not all energetic pulsars have been detected in all bands, it is generally accepted that this is mainly a result of the observers' orientation to the neutron star (NS) spin-axis. The radio and thermal X-rays in pulsars are thought to be emitted at low altitudes (the X-rays on the surface and the radio not very far from it), the result of dissipation of rotational energy into electric currents and particle acceleration. Because of its location, the X-ray emission has been considered as a reliable probe of NS masses

M_* and radii r_* , through the detailed modeling of the pulsar X-ray light curves, including the effects of photon propagation in the non-Minkowski metric of the NS (Lo et al. 2013; Miller & Lamb 2015). The precise determination of $\{M_*, r_*\}$ has been one of the goals of the *NICER* (Gendreau et al. 2016) mission. To this end, one of the first *NICER* targets has been the millisecond pulsar (MSP) PSR J0030+0451 (with a spin period of 4.865 ms), which is also a radio and a γ -ray pulsar, the first γ -ray MSP announced by *Fermi-LAT* (Abdo et al. 2009a).

Recently, two groups, Miller et al. (2019), Riley et al. (2019), hereafter M19 and R19, respectively, reported strong evidence for the existence of multipolar magnetic fields through modeling of the X-ray waveforms of PSR J0030+0451 that constrain $\{M_*, r_*\}$ to unprecedented accuracy. These results require the soft X-ray emitting areas on the NS surface to be both located in one rotational hemisphere while the observer direction lies in

Corresponding author: Constantinos Kalapotharakos
constantinos.kalapotharakos@nasa.gov
ckalapotharakos@gmail.com

the other hemisphere¹, with one spot being compact and the other a more elongated oval or crescent. Since these spots are thought to be generated by energetic particles from polar-cap pair-cascades (Harding & Muslimov 2001) or return currents (Contopoulos et al. 1999; Bai & Spitkovsky 2010; Kalapotharakos et al. 2014), such a configuration implies that the NS magnetic field cannot be a centered dipole, which would produce two near-circular antipodal polar caps (Abdo et al. 2009b; Bilous et al. 2019).

Pétri (2015, 2016) provided exact vacuum solutions of retarded fields for multipolar and offset dipole magnetic fields, respectively. Gralla et al. (2017) presented semi-analytic field structures that incorporate a superposition of centered dipole and quadrupole magnetic moments that are co-aligned. This configuration supports circular and annular polar caps the centers of which are antipodal. The imposed symmetries do not seem to be consistent with the results of M19; R19 for PSR J0030+0451.

Over the last decade, global macroscopic (Contopoulos & Kalapotharakos 2010; Bai & Spitkovsky 2010; Kalapotharakos et al. 2014) and kinetic particle-in-cell (PIC) (Cerutti et al. 2016; Philippov & Spitkovsky 2018; Kalapotharakos et al. 2018) pulsar magnetosphere models have determined that the main site of particle acceleration and MeV-GeV γ -ray emission is the equatorial current sheet (ECS) (although some emission can occur at high altitudes inside the light-cylinder (LC)), a fact supported by the recent discovery of the γ -ray pulsar Fundamental Plane (Kalapotharakos et al. 2019; Ploeg et al. 2020). The ECS is a characteristic feature of the force-free (FF) solutions (Contopoulos et al. 1999; Timokhin 2006; Spitkovsky 2006; Kalapotharakos & Contopoulos 2009) and forms outside the LC radius $R_{\text{LC}} = c/\Omega$.

The immediate question then is whether such a distorted, far from a pure centered dipolar, field geometry on the NS surface would manifest in the pulsar γ -ray light curves. While the location of the high-energy emission is generally considered remote (i.e., distant) from the NS surface, where the *NICER*-implied magnetic field distortions are important, the LC of PSR J0030+0451 is only $R_{\text{LC}} \approx 18r_*$ (assuming the *NICER* inferred radius of $r_* \approx 13$ km). To address this issue, Chen et al. (2020) presented recently a NS centered vacuum dipole-plus-offset-quadrupole magnetic field configuration, whose

footpoints on the NS surface roughly match the emission regions of R19. Adjusting the parameters of this general field make-up, they constructed a global FF magnetosphere model that produced γ -ray, radio, and X-ray light curves in modest agreement with observations. Their approach was driven mainly by the requirement that the centered dipolar component reproduce the γ -ray light curve. This led them to impose a magnetic dipole inclination angle of 80°.

In this paper, we take a different and more rigorous approach: We assume that the magnetic field comprises off-center dipole and quadrupole components and determine their parameters (i.e. positions, directions, relative strength) under static vacuum conditions, by demanding that the corresponding polar caps reproduce accurately the *NICER* X-ray light curve. This we achieve by employing a newly developed code, GIKS, that ray-traces photons in the Kerr-metric from a distant observer to the stellar surface hot-spots, for each choice of the magnetic field structure parameters. We also explore the corresponding parameter space of field configurations through a Markov Chain Monte Carlo (MCMC) code we have developed. We then turn the field configuration from static vacuum field (SVF) to force-free (FF) and implement the MCMC code to modify appropriately the field parameters so that the X-ray light curves of the FF configurations remain consistent with observation; for each such choice we also compute the corresponding γ -ray light curves and through their comparison with the *Fermi-LAT* ones we finally obtain an optimum set of magnetic field parameters consistent with both the X-ray and the γ -ray light curves. A significant nuance we consider is the proper phase synchronization of X-rays and γ -rays, which requires accounting for light travel time effects between the X-ray and the γ -ray emission regions.

In §2, we describe our codes and methodology and in §3 our results for the SVF and FF field configurations. Finally, in §4, we summarize the main conclusions, and in §5, we discuss the broader impacts and validity of our study as well as the future prospects.

2. METHODOLOGY

2.1. Geodesic Integration in Kerr Spacetime (GIKS)

Our ray-tracing code integrates an ensemble of individual photon trajectories that are placed on a uniform grid on a predefined sufficiently distant image (i.e., observer) plane with initial photon velocities perpendicular to that plane (similar to, but an independent implementation of, those detailed in Johannsen & Psaltis 2010; Psaltis & Johannsen 2012; Bauböck et al. 2012). This approach requires a much smaller number of integra-

¹ In this study, without loss of generality, we always consider that the observer is in the Northern rotational hemisphere (i.e., the hemisphere that is defined by $\boldsymbol{\Omega} \cdot \hat{\mathbf{n}} > 0$, where $\boldsymbol{\Omega}$ is the spin angular frequency vector and $\hat{\mathbf{n}}$ the normal vector at any point of the surface of the NS).

tions for a given density of trajectories that reach the image plane compared to an approach that integrates trajectories originating on the NS surface. We adopt a full Kerr-metric² but currently neglect stellar oblateness, which is expected to have smaller effects for the rotational frequency value of PSR J0030+0451³. The impact positions and zenith angles, ϑ_z , of the photons that reach the stellar surface are stored. The trajectories that hit the polar caps, which are assumed to be the hot-spot regions, are identified, taking into account the stellar rotation corresponding to the travel time of the individual photons. Doppler-boosting and emission anisotropy are incorporated by adopting photon weights on the image plane (Psaltis & Özel 2014). The light-curve intensity at a specific phase (i.e., observer time) is then derived by integrating over the image plane. The process is repeated for different phases that sample a complete period. The results are binned in phase identically to the binning of the observed X-ray light curve. We have verified our independent code on several test cases presented in Psaltis & Özel (2014); Bogdanov et al. (2019a).

In all the calculations below, we always use libraries of $\approx 2.5 \times 10^6$ photon trajectories that originate from an observer plane that is located at a distance of 300 Schwarzschild radii (i.e., $r_{\text{obs}} = 300r_s$, where $r_s = 2GM_*/c^2$) and reach the stellar surface⁴. We have verified the numerical fidelity of the model X-ray light curves due to the adopted r_{obs} value and the finite number of photon trajectories and it is well below the observational uncertainties for J0030+0451.

For our models of the PSR J0030+0451 X-ray profile, we fix M_* , r_* , and observer viewing angle, ζ , from the results of either M19⁵ or R19⁶. Moreover, M19 and

R19 reported that the temperatures of the two hot-spots are almost identical and so we assumed that all the hot-spots have the same temperature. Although the NICER inference codes used a fully ionized H atmosphere model, we currently implement, for simplicity, a $\cos^b \vartheta_z$ distribution for the emission from the hot-spots, where ϑ_z is the zenith angle and b the assumed anisotropy index. Exponents in the range $b \sim 0.5 - 1.0$ are a good approximation to the NSX atmosphere used by NICER (W. Ho, private Comm.). Testing different b values, for the hot-spot shapes corresponding to the highest likelihood parameter sets of M19 and R19, we found that the PSR J0030+0451 X-ray profile is reproduced for $b = 0.65$ and $b = 1.0$, respectively. We note that M19 used channels 40 - 299 (0.4 - 3 keV) while R19 included NICER energy channels 25 - 299 (0.25 - 3 keV) in their analyses.

2.2. Markov Chain Monte Carlo Exploration

We have developed an MCMC code⁷ that computes likelihoods for the walker steps corresponding to different field parameters (i.e., different field structures and therefore, different hot-spots) for the NICER bolometric (0.25 - 1.45 keV) X-ray profile from Bogdanov et al. (2019b). We defer the full energy-dependent analysis for a future work.

The adopted field model configuration is the superposition of static dipole and $m = 0$ quadrupole moments whose orientation and offsets (from the center of the NS) are allowed to vary. Flat distributions are considered for all the priors while the radial offsets are limited to not exceed $0.7r_*$. The dipole and quadrupole fields, in spherical magnetic coordinates, read

$$\mathbf{B}_D = B_D \left(\frac{r_*}{r_D} \right)^3 \left\{ \cos \theta_D, \frac{1}{2} \sin \theta_D, 0 \right\} \quad (1)$$

$$\mathbf{B}_Q = B_Q \left(\frac{r_*}{r_Q} \right)^4 \left\{ \frac{1}{2}(3 \cos^2 \theta_Q - 1), \cos \theta_Q \sin \theta_Q, 0 \right\} \quad (2)$$

where r_D , r_Q are the corresponding radial distances from the moment locations and θ_D , θ_Q the corresponding magnetic co-latitudes.

The determination of the magnetic field configuration requires ten parameters. More specifically, two for the position of the dipole moment relative to the star center (at some fixed azimuth), three for the position of the quadrupole moment relative to the dipole moment, four angles that determine the orientation of the dipole and quadrupole moments with respect to Ω , and

² We note that even though GIKS code incorporates the Kerr spacetime the corresponding frame-dragging effects in this type of problem are actually negligible, which implies that our results are practically consistent with Schwarzschild spacetime. A more rigorous approach would require the implementation of a spacetime (i.e., metric) that is the result of the numerical solution of the corresponding full Einstein equations with a specified equation of state.

³ The ellipticity for the rotational frequency of PSR J0030+0451 is expected to be $\lesssim 6 \times 10^{-3}$ (Bauböck et al. 2013).

⁴ A value for the observer distance 10 times higher does not affect the results.

⁵ We considered the two oval model. Nonetheless, we note that M19 also presented a model with three hot-spots in which the smallest hot-spot had a different (i.e., larger) temperature than the other two but due to its location and size had minor contribution. This model was only marginally statistically preferred compared to the one with the two equal-temperature oval shaped hot-spots.

⁶ We considered the best model (i.e., ST+PST).

⁷ A custom Fortran code with serial and MPI-parallel implementations of a stretch move of Goodman & Weare (2010).

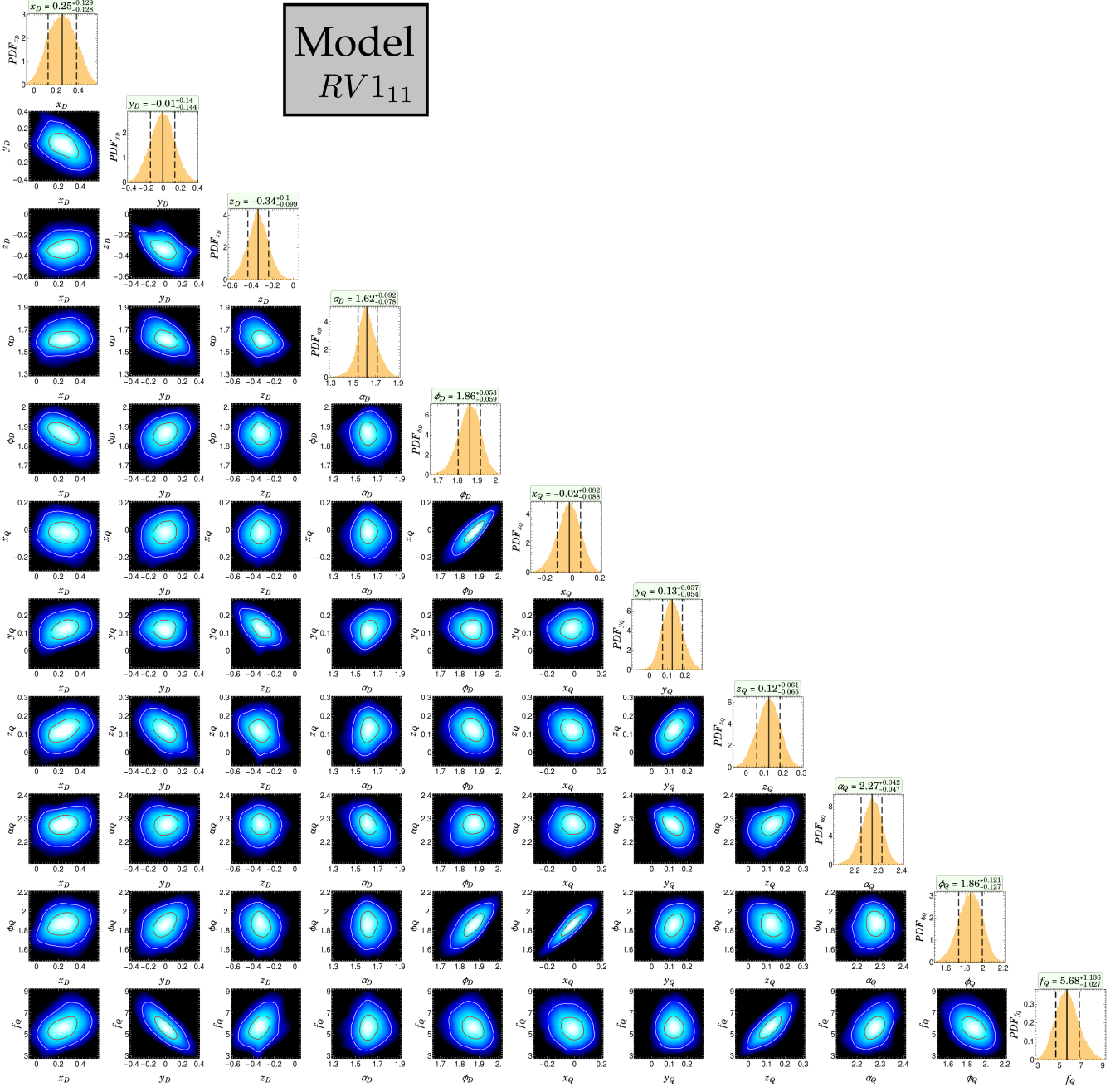


Figure 1. The corner plot, produced by the MCMC exploration corresponding to the model *RV111*. All the possible 2D posterior probability density distributions are shown in density plots from low (black) to high (white) values. The two lines in each panel denote the 1σ and 2σ regions. The marginalized 1D posterior probability distributions for the 11 parameters are shown along the diagonal. The solid lines denote the corresponding mean values while the dashed lines denote the 68% containment regions. The median and $\pm \sigma$ values for each parameter are shown above the corresponding 1D plot.

the Ω -observer plane, and the relative strength of the quadrupole moment (i.e., $f_Q \equiv B_Q/B_D$) at a distance that is equal to the NS radius. Thus, without regard for absolute phasing, ten parameters describe the fields. However, for a finite distance between the star and the image plane, the absolute azimuth of the dipole moment is also set by the presumed zero phase point (e.g. from radio) of the X-ray light curve.

Thus, eleven free parameters are explored by the MCMC, which are the three Cartesian position coordinates $\{x_D, y_D, z_D\}$, the inclination α_D and the azimuth direction ϕ_D of the dipole moment, the corresponding three Cartesian position coordinates $\{x_Q, y_Q, z_Q\}$, the inclination α_Q and the azimuth direction ϕ_Q of the quadrupole moment, and the f_Q ratio. We note that the Cartesian coordinates are measured with respect to the

Table 1. Parameters corresponding to the highest likelihood for the SVF models. For the *RV* models, we adopted the R19 median values (of the corresponding posterior distribution) for the stellar mass $M_\star = 1.34M_\odot$, radius $r_\star = 12.71\text{km}$, and the observer angle $\zeta = 53.85^\circ$. Similarly, for the *MV* models, we adopted the M19 best fit values $M_\star = 1.49M_\odot$, $r_\star = 13.64\text{km}$, and $\zeta = 47.38^\circ$. We emphasize that the compactness (M_\star/r_\star) between the *RV* and *MV* models are much closer to each other compared to the corresponding individual M_\star and r_\star values.

| Quantity | <i>RV</i> 1 ₁₁ | <i>RV</i> 2 ₁₁ | <i>RV</i> 3 ₁₁ | <i>RV</i> 4 ₁₁ | <i>RV</i> 5 ₈ | <i>RV</i> 6 ₆ | <i>MV</i> 1 ₁₁ | <i>MV</i> 2 ₁₁ | <i>MV</i> 3 ₁₁ | <i>MV</i> 4 ₁₁ | <i>MV</i> 5 ₈ | <i>MV</i> 6 ₆ |
|-------------------------|---------------------------|---------------------------|---------------------------|---------------------------|--------------------------|--------------------------|---------------------------|---------------------------|---------------------------|---------------------------|--------------------------|--------------------------|
| $x_D(r_\star)$ | 0.12 | 0.17 | 0.45 | -0.20 | 0.00 | 0.00 | 0.26 | 0.26 | 0.07 | 0.34 | 0.00 | 0.00 |
| $y_D(r_\star)$ | -0.17 | 0.39 | 0.29 | 0.46 | 0.00 | 0.00 | 0.12 | 0.22 | -0.36 | -0.21 | 0.00 | 0.00 |
| $z_D(r_\star)$ | -0.30 | -0.04 | 0.11 | -0.25 | 0.00 | 0.00 | 0.24 | -0.35 | -0.24 | -0.40 | 0.00 | 0.00 |
| $\alpha_D(\text{rad})$ | 1.75 | 1.60 | 1.98 | 1.53 | 1.00 | 1.38 | 1.38 | 1.72 | 1.29 | 1.45 | 1.40 | 1.35 |
| $\varphi_D(\text{rad})$ | 1.94 | 2.19 | 2.21 | 4.60 | 1.82 | 1.94 | 2.56 | 2.56 | 5.79 | 2.60 | 2.63 | 2.53 |
| $x_Q(r_\star)$ | 0.07 | 0.40 | 0.16 | 0.31 | 0.62 | 0.00 | 0.09 | 0.06 | -0.23 | -0.36 | 0.09 | 0.00 |
| $y_Q(r_\star)$ | 0.14 | 0.22 | -0.17 | -0.13 | 0.20 | 0.00 | 0.16 | 0.17 | -0.37 | 0.36 | 0.19 | 0.00 |
| $z_Q(r_\star)$ | 0.07 | -0.12 | -0.38 | -0.15 | -0.20 | 0.02 | -0.17 | -0.18 | -0.25 | -0.09 | -0.17 | -0.16 |
| $\alpha_Q(\text{rad})$ | 2.18 | 2.29 | 0.60 | 1.68 | 0.92 | 0.75 | 2.34 | 2.18 | 2.04 | 2.60 | 2.38 | 2.42 |
| $\varphi_Q(\text{rad})$ | 1.90 | 2.45 | 6.06 | 4.94 | 5.78 | 4.89 | 2.69 | 2.72 | 0.07 | 2.17 | 2.65 | 2.35 |
| B_Q/B_D | 5.58 | 5.01 | 2.39 | 3.22 | 8.69 | 6.38 | 4.97 | 3.58 | 8.10 | 0.93 | 4.81 | 5.17 |
| χ^2_r | 0.66 | 0.60 | 0.71 | 0.78 | 0.58 | 0.85 | 0.70 | 0.72 | 1.36 | 1.67 | 0.68 | 0.80 |

NOTE—Prefixes: R – Riley, M – Miller, V – static vacuum fields

center of the star, the inclination angles with respect to Ω , and the azimuth direction angles with respect to the x axis oriented with Ω . In this configuration the observer always lies on the $x-z$ plane. The eleven parameters described above define the magnetic field configuration (at the assumed distance from the image plane) at the moment the observer receives the zero-phase photons. To clarify, the “picture” the observer observes at the time corresponding to the zero-phase photon is different (due to the r_{obs}/c travel time) from what the field parameter values dictate (see also Fig. 8 and the related discussion in Section 3.3.2).

In each MCMC step, the polar cap corresponding to the field structure, determined by a point of the eleven dimensional parameter space, is calculated, and then the model X-ray light curve is derived using the library of photon trajectories that has been produced by GIKS. Comparison of the model to the observed X-ray light curve then provided the likelihood value and the corresponding χ^2 value. We note that the adopted background level of the NICER X-ray light curve has been chosen to be consistent with the background level depicted in M19. Thus, the signal reads $N_S = N_T - N_B$, where N_S , N_T , and N_B are the source, total, and background photon counts, respectively. The adopted uncertainties for N_T and N_B are considered Poisson type (i.e., $\sqrt{N_i}$, where N_i is the number of observed counts in the i^{th} bin out of the 64 phase bins). Therefore, the un-

certainty of the source photon count is $\sigma_S = \sqrt{\sigma_T^2 + \sigma_B^2} = \sqrt{N_T + N_B}$.

Finally, we note that assuming equal hot-spot temperatures, the normalization of our model photon weights for the X-ray flux is determined using the reported model hot-spot shapes from M19 and R19, which reproduce the bolometric light curves for $b = 0.65$ and $b = 1.0$, respectively (see end of section 2.1).

3. RESULTS

3.1. Model Nomenclature

In this section, we present our results adopting the findings of R19 assuming both SVF and FF field structures and the findings of M19 assuming SVF structures. We note that our models are named ABn_m , where $A = (R, M)$ indicates the adopted fixed parameters (R19 or M19), $B = (V, F)$ indicates the assumed field structure, static vacuum field (SVF) or force-free (FF), n describes the number of the corresponding AB model, and m indicates the dimensionality of the corresponding field parameter space.

3.2. Vacuum Fields

In the first step, we explored the parameter space assuming that the global magnetosphere structure is described by an SVF. Since the SVFs are described by analytic expressions, the rapid calculation of the polar

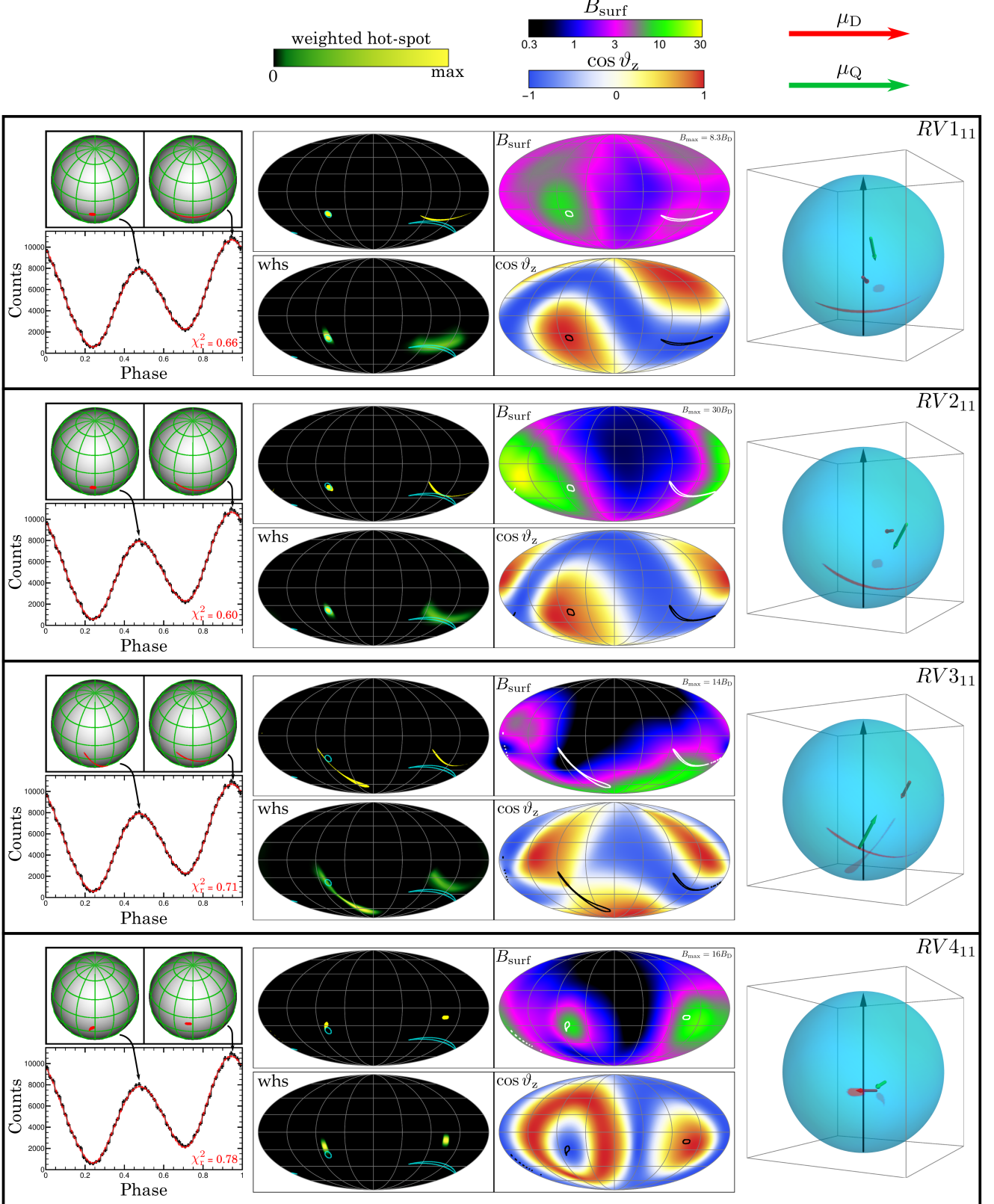


Figure 2. The characteristics of the four RV models with eleven free parameters. Each row (inside the thick black frame) corresponds to the indicated model. In the first column, the bottom panel shows the observed *NICER* X-ray light curve (black line with error-bars) together with the corresponding model X-ray light curve (red color). The corresponding χ^2_r values are depicted in the panels. (Continued in the next page)

Figure 2. (Continued) The two top panels depict the image plane, with limb darkening, at the indicated phases (i.e., the primary and secondary maxima). The top panels in the second column depict the model hot-spots (i.e., polar caps) in yellow color on the Mollweide projection of the stellar surface. The bottom panels show, in the indicated color scale, the superposition of hot-spot regions from the entire corresponding posterior distribution (i.e., weighted hot-spots). In both panels, the cyan lines denote the hot-spot regions denoted by R19. The top panels of the third column depict, in the indicated color scale, the strength of the surface magnetic field. The corresponding maximum strength is also indicated. The bottom panels depict, in the indicated color scale, the cosine of the zenith angle of the magnetic field on the stellar surface. The model hot-spots are indicated in the top and bottom panels by the white and black lines, respectively. The fourth column schematically depicts (in flat spacetime) the locations of the dipole (red arrow) and the quadrupole (green arrow) magnetic moments inside the star. The locations of the moments are at the middle of the plotted arrows. The black arrows indicate Ω . The corresponding model polar caps (red areas) are also depicted on the transparent stellar surface.

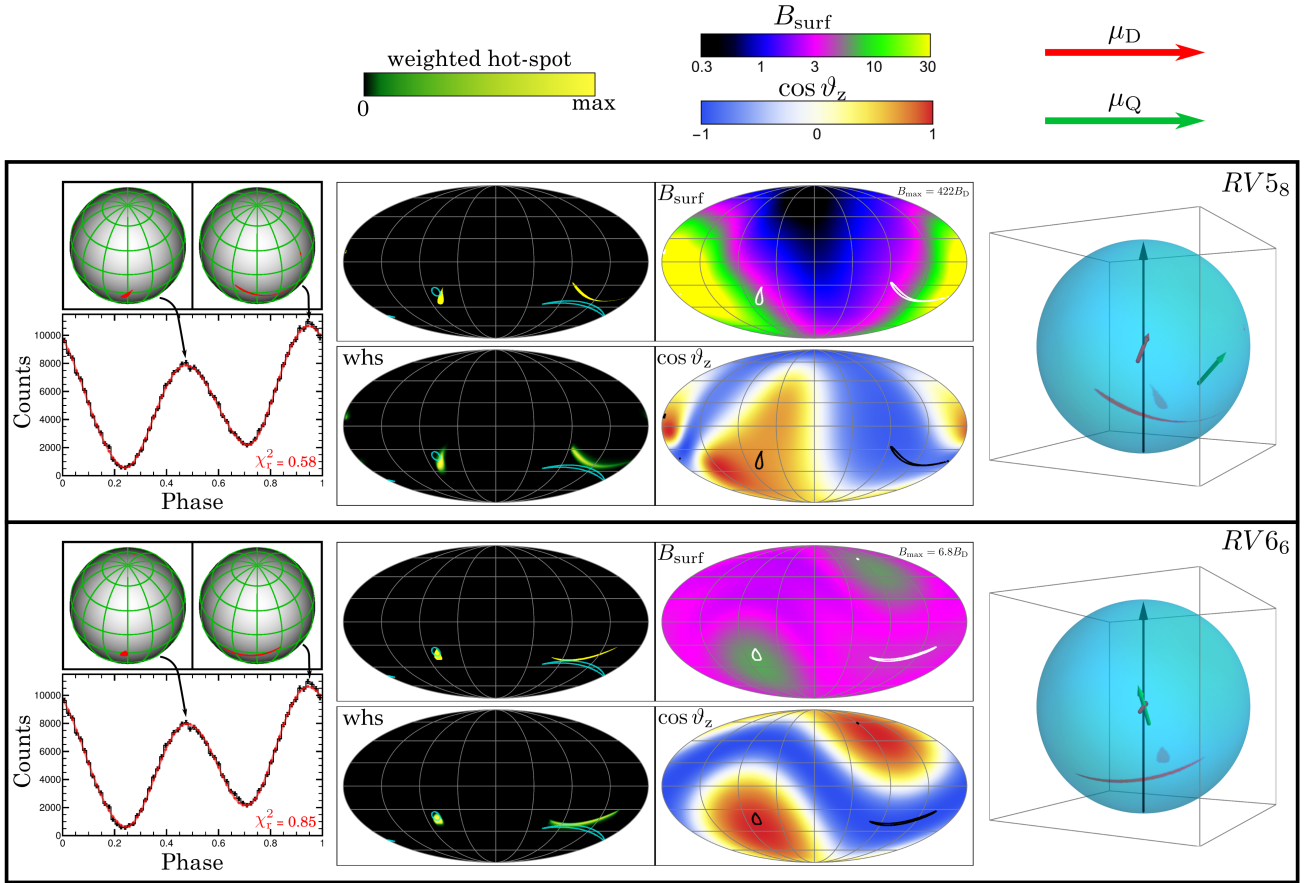


Figure 3. Similar to Fig. 2 but for the RV models with 8 and 6 free parameters.

caps allows both a test of our methodology and a more thorough exploration of the parameter space on the order of seconds per likelihood evaluation.

We separately ran 2000 independent serial MCMC chains each of which started from different random initial positions, in the parameter space.

The average number of accepted MCMC steps (according to the corresponding likelihood ratios) in each of these chains was ~ 800 . This exploration located distinct islands in the multidimensional parameter space with high likelihood. We then ranked the likelihood values of these distinct islands and selected the four highest

locales, which represent local maxima in a multimodal landscape.

We then thoroughly explored the islands individually, using the parallel version of the MCMC code. In each of these MCMC explorations, the total number of accepted points, excluding the burn-in period, were $\sim 4 \times 10^5$.

Moreover, following a similar process, we studied models with restricted priors. More specifically, we fixed the dipole moment at the center of the NS and additionally also restricted the quadrupole moment along the spin axis. In these cases, the dimensionality of the parameter space is reduced from 11 to 8 and 6, respectively.

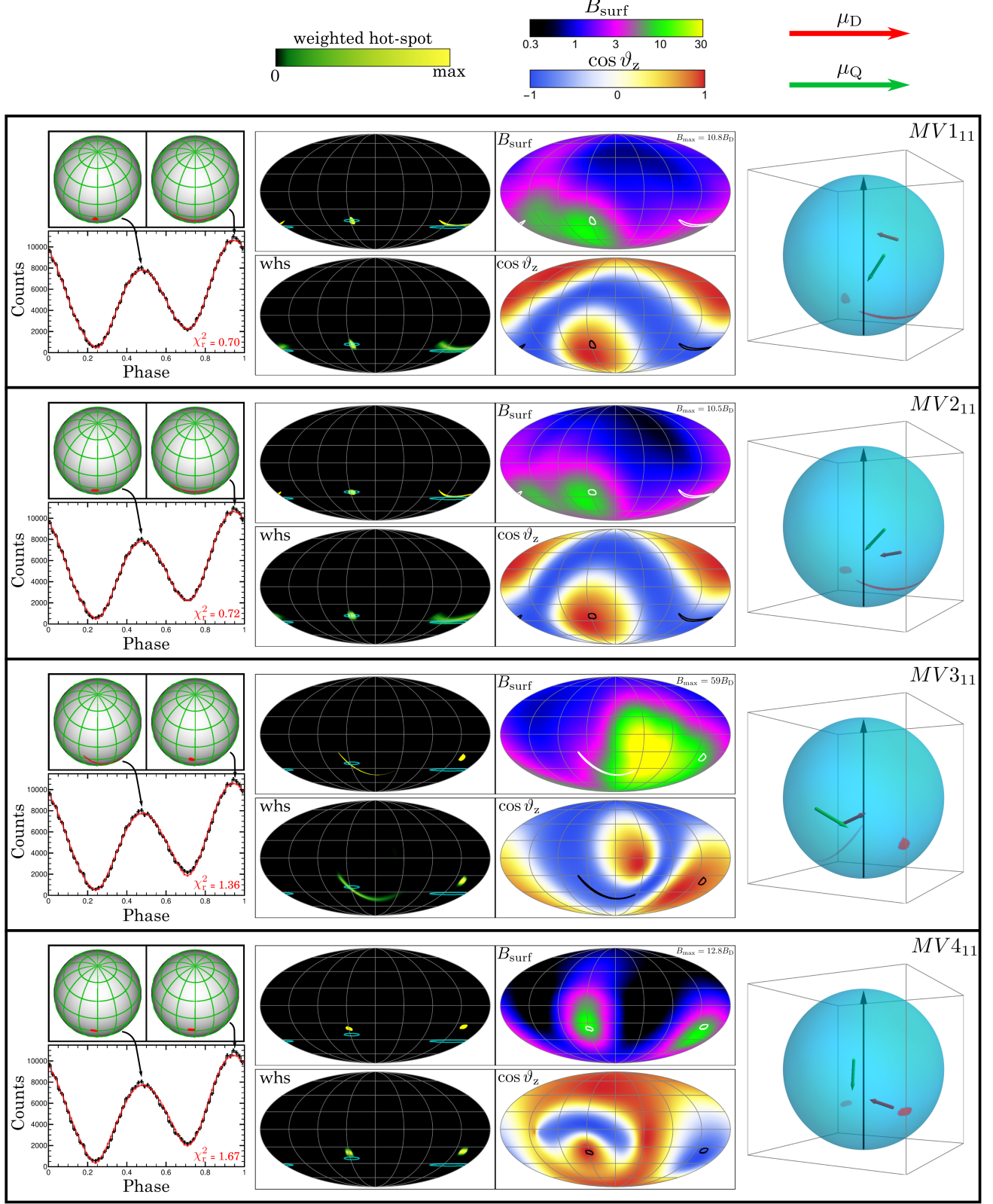


Figure 4. Similar to Fig. 2 but for the MV models with 11 free parameters. The cyan lines in the second column denote the hot-spot regions denoted by M19. We note that the apparent phase difference between the R19 hot-spots shown in Figs. 2–3 and the M19 ones shown in Figs. 4–5 is due to the different adopted r_{obs} values (recall that $r_{\text{obs}} = 300r_s$ and therefore, different in the two cases).

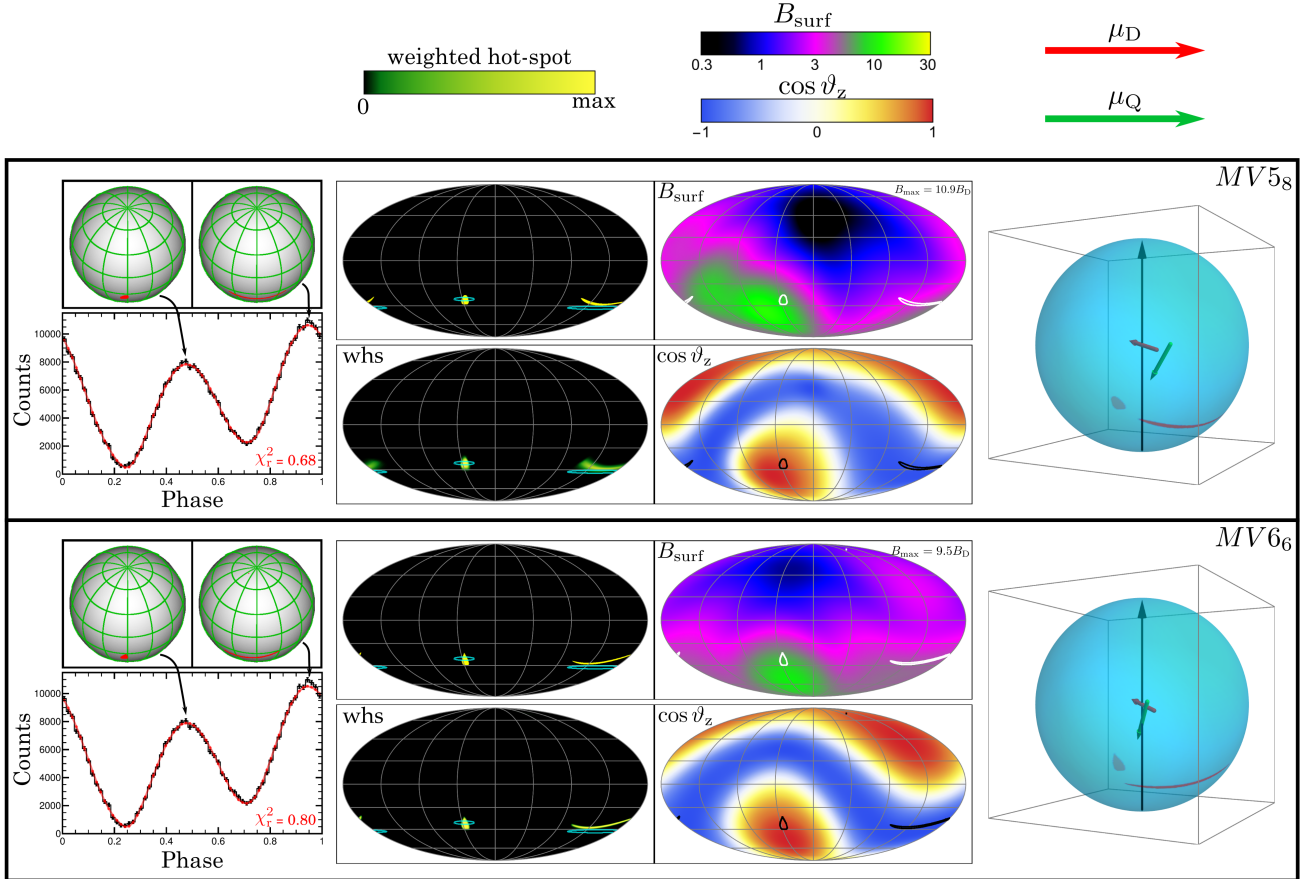


Figure 5. Similar to Fig. 4 but for the *MV* models with 8 and 6 free parameters.

In Table 1, we present the model parameters for a total of twelve (six adopting the [R19](#) median M_* , r_* , and ζ values and six adopting the [M19](#) best fit ones) cases. The fifth and sixth parameter sets (i.e., *RV*₅₈, *MV*₅₈, *RV*₆₆, *MV*₆₆) are the highest likelihood models for the centered dipole plus free quadrupole and for the centered dipole plus z -axis quadrupole. The last row shows the corresponding reduced χ^2 values, $\chi^2_r = \chi^2/\text{dof}$ where dof are the degrees of freedom, which in our case is dof = $n - k$, where $n = 64$ the number of bins and k the dimensionality of the parameter space. We note that the specific parameter values that are presented in all the Tables have been calculated using a surface resolution 5000×5000 for the hot-spot determination while the surface resolution that was used for the calculations that concluded to the posterior distributions (e.g., Fig. 1) was 600×600 . The determination of hot-spots is made by the identification of the open magnetic field lines (i.e., those that cross the LC). For the identification of the open magnetic field lines, we integrate, using an adaptive Runge-Kutta 4–5 method, 5000×5000 (or 600×600) field lines uniformly distributed on the stellar surface. A bilinear interpolation is then used to describe the entire stellar surface. The errors

in fidelity of the model X-ray light curves due to the 600×600 discretization are well below the observed uncertainties (while for 5000×5000 are negligible). We also note that in the current study, we have calculated the fields in the Euclidean space⁸.

All the models describe the bolometric *NICER* X-ray light curve extremely well. It is noted though that the *MV* models seem to have slightly higher χ^2_r values than those of the *RV* ones.

In Fig. 1, we present the eleven parameter corner plot for the *RV*₁₁. The density-plots show, in color-scale, the projected distributions on the corresponding 2D subspaces. The red and white lines denote the 1σ and 2σ regions, respectively. Along the diagonal the histograms of the marginalized 1D projections of the 11-dimensional parameter-space are plotted. The solid and dashed lines

⁸ Assuming a pure centered dipole, the field direction inside the corresponding polar cap on the stellar surface of PSR J0030+0451 is diverted by $\lesssim 0.5^\circ$ due to the corresponding Schwarzschild spacetime distortions ([Wasserman & Shapiro 1983](#); [Gonthier & Harding 1994](#)). The diversion of the field direction decreases almost inversely proportional to the r/r_* .

denote the median and 1σ values, which are also shown above the histogram panels.

In Figs. 2–3, we present the characteristics for all six *RV* models from Table 1. The first column shows the model X-ray light curve (red line) together with the observed one (black points and error-bars). The image planes corresponding to the indicated light-curve peaks are also depicted. The hot-spot (i.e., emitting) regions are the red areas. We note that the gray color-scale denotes the adopted emission anisotropy. In the top panel of the second column, the model hot-spots (yellow areas) corresponding to the highest-likelihood parameter sets are plotted on the stellar surface Mollweide projection. The areas within the cyan lines denote the hot-spot areas of R19. The bottom panel of the second column presents, in the indicated color-scale, the weighted (according to the corresponding posterior probability distributions) model hot-spots. The third column shows properties of the magnetic field structure on the projected stellar surface. The top and bottom panels present, in the indicated color-scales, the magnitude B_{surf} and cosine of the zenith angle (i.e., $\cos \vartheta_z$) of the magnetic field. The highest values of the corresponding magnetic fields (in units of the centered dipole field on the stellar surface) are indicated in the top panels. The white and black lines in these plots denote the corresponding hot-spots. The last column shows the locations and directions of the corresponding dipole moment (red arrow) and quadrupole moment (green arrow). Finally, Figs. 4–5 are similar to Figs. 2–3 but for the *MV* models (see Table 1).

Our results show a degeneracy of the field structures that can reproduce the bolometric X-ray light curve of PSR J0030+0451. It is also evident that quite different field parameters can provide similar hot-spot regions on the stellar surface (see [*RV*₂₁₁, *RV*₅₈], [*RV*₁₁₁, *RV*₆₆], and [*MV*₁₁₁, *MV*₂₁₁, *MV*₅₈, *MV*₆₆] model family groups). Many hot-spots of our models share common features to those presented by M19 and R19. Thus, the left-hand hot-spot is often more compact and circular while the right-hand is elongated. However, the elongated hot-spots in our models always form a “smiley” face while M19’s and R19’s ones form a neutral and “frowny” faces, respectively⁹. The difference of the hot-spot shapes between M19 and R19 was indicative of the underlying degeneracy as well as their

different adopted shape geometries. Moreover, there are cases in our models where the hot-spots are quite dissimilar qualitatively than those of M19 and R19.

The maximum field value on the stellar surface in our models ranges from ~ 7 to $\sim 400B_D$. The quadrupole strength is higher than the dipole one with only one exception (i.e., *MV*₄₁₁). For eleven (out of the twelve) cases the f_Q ratio is $f_Q \gtrsim 2.4$ while for the eight of them it is $f_Q \gtrsim 4.8$. The f_Q values corresponding to parameter spaces with lower dimensionality (i.e., *RV*₅₈ *RV*₆₆ *MV*₅₈ *MV*₆₆) are always $f_Q \gtrsim 5$.

3.3. Force-Free Plasma Models

3.3.1. The NICER X-ray Light Curve

The SVF solutions are instructive and helpful for code testing, but FF and dissipative magnetosphere models with currents and charges are much closer to those of real pulsars. Furthermore, such models have the ability to show the distributions of currents of different signs and values on the polar caps, which are physically important for constraining the pair-cascades and heating of the polar caps (i.e., hot-spots). Dissipative magnetospheres with accelerating electric field components also enable us to compute γ -ray emission light curves. Having determined the SVF configuration that reproduces the *NICER* X-ray profile, these parameter values were used as initialization coordinates for the serial MCMC to find the best parameter FF solution for a dipole plus quadrupole field configuration, again fixing the M_* , r_* , and ζ values from the *NICER* results.

We have incorporated the FF magnetosphere simulator (Kalapotharakos et al. 2012, 2014) inside our MCMC code as a module for likelihood evaluation. The MCMC part of the code dictates the magnetic field parameter values that are explored and the FF simulator provides the corresponding magnetosphere structure. The set of the field parameter values define the field boundary conditions on the stellar surface. The magnetic field inside the star that is determined in principle by the sum of the offset dipole and quadrupole moments while the electric field is defined by $\mathbf{E} = -(\boldsymbol{\Omega} \times \mathbf{r}) \times \mathbf{B}/c$.

The derivation of the FF field structure has a much higher computational overhead (of order $\sim 10^2$ times more CPU time per likelihood evaluation) than the analytic static vacuum field models. Each FF field module runs in parallel using 12^3 processors and therefore, the MCMC exploration is serially performed (i.e., at every MCMC step only one point in the parameter space is explored). The FF simulations implement a grid resolution $0.04R_{\text{LC}}$, which does not allow a simulation stellar surface of radius smaller than $r_{\text{sim}} = 0.25R_{\text{LC}}$. However, even though this stellar radius is four to five times

⁹ A detailed exploration of the parameter space has shown that there are regions of rather limited hypervolume in the parameter space that allow wavy hot-spot shapes that contain a significant “frowny” component. Nonetheless, none of these can adequately describe the bolometric X-ray light curve.

Table 2. Parameters corresponding to the highest likelihood for the FF models.

| Quantity | $RF1_{11}$ | $RF2_{11}$ | $RF3_{11}$ | $RF4_{11}$ | $RF5_8$ | $RF6_6$ |
|-------------------------|------------|------------|------------|------------|---------|---------|
| $x_D(r_*)$ | 0.16 | 0.26 | 0.48 | -0.13 | 0.00 | 0.00 |
| $y_D(r_*)$ | -0.21 | 0.29 | 0.23 | 0.60 | 0.00 | 0.00 |
| $z_D(r_*)$ | -0.38 | -0.10 | 0.09 | -0.21 | 0.00 | 0.00 |
| $\alpha_D(\text{rad})$ | 1.65 | 1.41 | 1.89 | 1.30 | 1.02 | 1.45 |
| $\varphi_D(\text{rad})$ | 2.01 | 2.26 | 2.28 | 4.82 | 2.11 | 1.97 |
| $x_Q(r_*)$ | 0.05 | 0.32 | 0.19 | 0.37 | 0.60 | 0.00 |
| $y_Q(r_*)$ | 0.15 | 0.25 | -0.18 | -0.35 | 0.14 | 0.00 |
| $z_Q(r_*)$ | -0.08 | -0.24 | -0.37 | -0.27 | -0.28 | -0.12 |
| $\alpha_Q(\text{rad})$ | 2.21 | 2.30 | 0.59 | 1.48 | 0.88 | 0.79 |
| $\varphi_Q(\text{rad})$ | 1.92 | 2.46 | 5.97 | 4.83 | 5.75 | 4.91 |
| B_Q/B_D | 5.97 | 5.42 | 3.15 | 2.12 | 9.82 | 6.86 |
| χ^2_r | 0.92 | 0.85 | 1.13 | 0.93 | 1.50 | 8.94 |

NOTE—Prefixes: R – Riley, F – force-free fields

larger than the actual one, it is still well inside the LC. Eventually, the determination of the polar caps on the corresponding actual stellar radius, r_* , takes into account the field structure outside $r_{\text{sim}} = 0.25R_{\text{LC}}$ and the corresponding SVF structure inside the stellar surface. The numerical FF solution (outside r_{sim}) is smoothly joined to the SVF (inside r_{sim}) through a linear ramp function.

Severe computational limitations do not allow a detailed exploration of the parameter space for the FF regime, which would allow the determination not only of the highest likelihood parameters but also of the corresponding posterior distributions (e.g., corner plots). Nonetheless, we ran in total 12 MCMC chains, 6 starting from the highest likelihood parameter values of the RV models and another 6 starting from different parameter values (i.e., not corresponding to the highest-likelihood values) of the RV models. In each of these runs, we explored several hundreds to a few thousand points of the parameter space while the accepted number of MCMC points were of the order of a few hundred. The exploration in each of these MCMC chains continued until either a likelihood value corresponding to $\chi^2_r \lesssim 0.8$ was found or a few thousand points in the parameter space had been explored. Even though the accepted number of points were inadequate to provide proper posterior distributions, they were enough to provide likelihood values close to the corresponding local maxima. Thus, in the FF cases, the MCMC approach was mainly used as an optimization method.

In Table 2, we present the highest likelihood model parameters for six FF models. Each RF_n model is the

highest likelihood FF model among the models corresponding to the 2 MCMC chains we ran for each RV_n model. Our results show that the first five models ($RF1_{11} - RF5_8$) have adequately low χ^2_r values (i.e., of the order of 1) and acceptably describe the data.

In the left-hand column of Figs. 6–7, we plot the FF X-ray light curves having the highest likelihood while in the middle column, we plot the corresponding hot-spot regions on the projected stellar surface. We see that the hot-spot patterns are very similar to the corresponding RV models, which implies that the RF models represent the same hot-spot families in the FF regime. However, the areas of the FF hot-spot regions are, in general, larger than those in SVF¹⁰. Moreover, we note that a by-eye comparison indicates that the $RF6_6$ model X-ray light curve is quite close to the observed light curve and the corresponding high χ^2_r value is due to the very small observational uncertainties.

For the $RF6$ model, we explored ~ 4000 points in the parameter space getting ~ 160 accepted points in the MCMC chain. The likelihood values stabilized to the ones quoted in Table 2. Nonetheless, as is an issue with all higher-dimensional search problems, the limited number of accepted points leaves unclear whether these optimized likelihoods are a global maximum.

¹⁰ It is well known from the pure central dipole solutions that the FF polar caps are larger and shifted compared to those in the corresponding vacuum ones. This is because the flowing currents not only increase the escaping magnetic flux but the field lines are also swept back due to rotation.

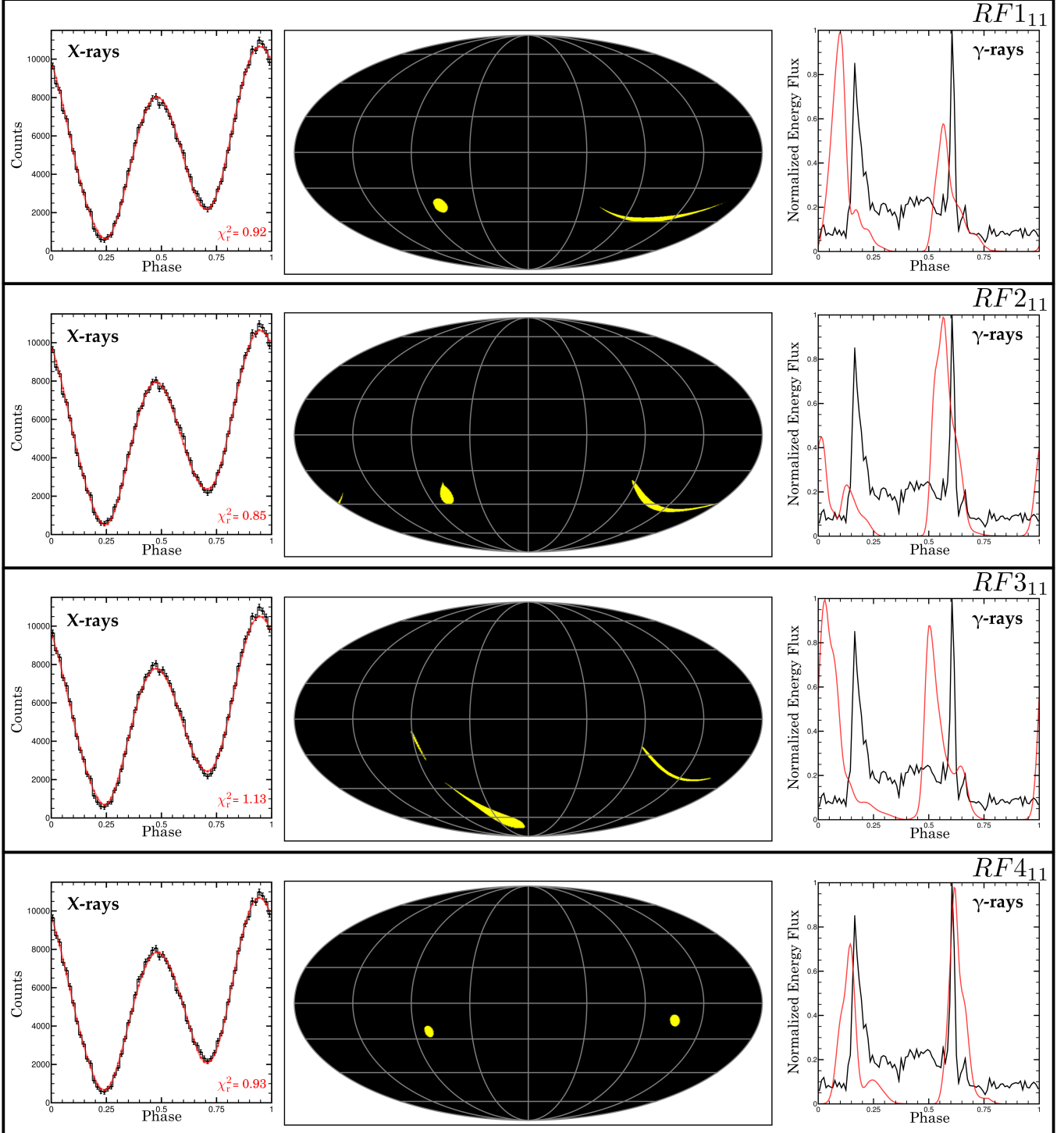


Figure 6. The RF models with 11 free parameters. Each row corresponds to the indicated RF model. The left-hand panels show the *NICER* X-ray light curve (black lines with error-bars) together with the FF model X-ray light curve (red color). The corresponding χ^2_r value are also denoted. The middle panels show the corresponding hot-spots (yellow regions) on the stellar surface. The right-hand panels show the *Fermi-LAT* γ -ray light curve (black line) together with the model γ -ray light curve (red line).

3.3.2. *Fermi-LAT* γ -ray Light Curve

Our results indicate field degeneracies for both the SVF and FF models. Even though the observed X-ray

light-curve sets constraints there are many different field structures that may adequately describe the bolometric *NICER* X-ray light curve. There are not only differ-

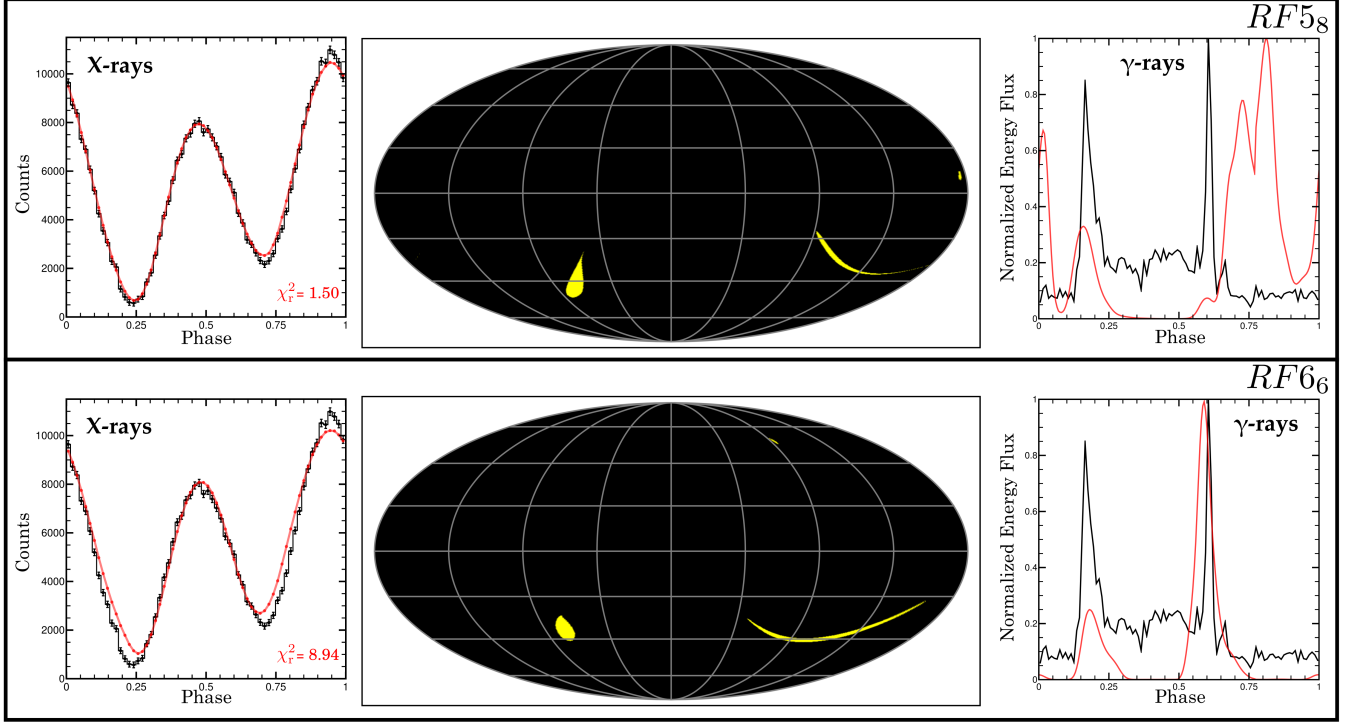


Figure 7. Similar to Fig. 6 but for the RF models with 8 and 6 free parameters.

ent field parameters corresponding to different hot-spot families (e.g., RVn and RFn families) of quite different hot-spot patterns but also quite different field parameters within the same families (see Fig. 1). Even though there are models with higher and lower χ^2_r values, the actual χ^2_r values, for the majority of the models, are of the order of unity and therefore, they are all statistically acceptable, although some may be formally preferred, e.g. by an F-test. Yet, as we show below, more pertinent is whether the solutions can correctly describe the phasing of the γ -ray light curves.

The variation of the magnetic field parameters affect the magnetic field structure even near the LC. Usually at large distances, the magnetic field geometry is dictated by the dipole moment parameters. However, in MSPs like PSR J0030+0451 the corresponding R_{LC} lies at only $\approx 18r_*$, which implies that the magnetic moment offsets, and the quadrupole strength would significantly affect the field structure of the outer magnetosphere i.e., near the LC. The offsets and the f_Q ratio would actually introduce deviations of the field structure from central symmetry.

The field structure geometry in the outer magnetosphere and especially near and beyond the LC affects the locus of the ECS and therefore, the corresponding γ -ray emission. Assuming a pure centered dipole field, the γ -ray emission observed by *Fermi-LAT* sets con-

straints on α and ζ (i.e., the only parameters involved) although there are degeneracies.

The statistical quality of the X-ray signal is very high for all phases in contrast to the γ -rays, and therefore, an accurate reproduction of the X-ray light curve is required. On the other hand, the phases of γ -ray peaks set constraints mainly on the locus of the ECS, which is strongly related to the field structure parameters. Other morphological characteristics of the γ -ray light curves are less related to the field geometry. For instance, the width of the pulses is mainly related to the width of the dissipative magnetosphere region while the inter-peak and off-peak emission is mainly related to the emission that is produced inside the LC.

In Kalapotharakos et al. (2014), we introduced the so-called FIDO models that reproduce the observed correlation between the radio-lag, δ and peak-separation, Δ of young pulsars. In Brambilla et al. (2015); Kalapotharakos et al. (2017), we expanded and generalized the FIDO models revealing the dependence of the plasma conductivity on the spin-down power $\dot{\mathcal{E}}$ that reproduce not only the $\delta - \Delta$ correlation but also the observed *Fermi-LAT* spectra. In the FIDO model the γ -ray emission that is produced near the ECS is due to curvature radiation (CR).

In this study, we adopt the approach we had followed in (Kalapotharakos et al. 2014) for the derivation of the model γ -ray light curves. We use the FF solutions

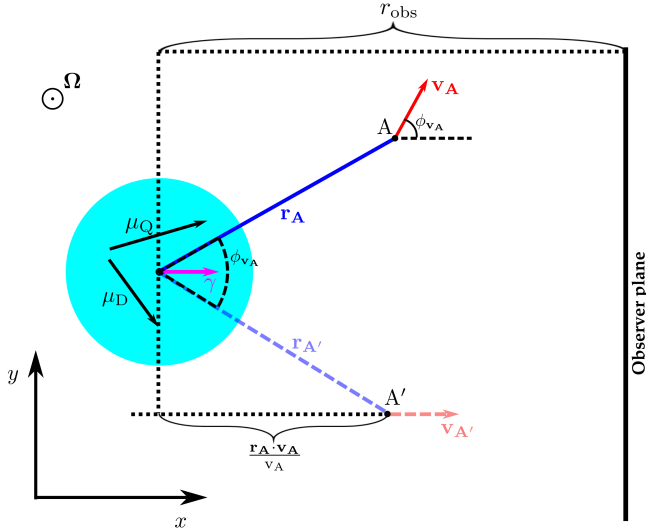


Figure 8. Schematic diagram, set in the equatorial plane for clarity, illustrating the self-consistent astrocentric time coordinates and synchronization of surface X-rays and magnetospheric γ -rays.

adopting an accelerating electric field component that reads

$$E_{\parallel} = \frac{c(\nabla \times \mathbf{B}) \cdot \hat{\mathbf{B}}}{4\pi\Sigma_c} \quad (3)$$

where $\hat{\mathbf{B}}$ is the local magnetic field unit vector and Σ_c is the plasma conductivity. We have adopted $\Sigma_c = 1\Omega$ constant everywhere; we note, however, that the exact Σ_c value mainly affects the spectra and not the γ -ray light curves as long as Σ_c is high enough to produce a nearly-FF field solution.

We integrated test particle trajectories, using a 4th order Runge-Kutta with constant step-size, that originate near the separatrices of the open and closed field lines. More specifically, for each *RF* model, we calculated the polar-cap rims at $r = 0.5R_{LC}$ and we integrated 10^6 test particle trajectories that originate at $r_{tr} = 0.5R_{LC}$ within an angle 3° from the corresponding polar-cap rim. The particle trajectories follow the Aristotelian electrodynamics¹¹ (Gruzinov 2012; Kelner et al. 2015; Jacobson 2015) and the particle energies are determined by both the energy gains due to the encountered E_{\parallel} and the energy losses due to CR. A detailed description of the methodology is in Kalapotharakos et al. (2014) and Kalapotharakos et al. (2017). The E_{\parallel} and radiation energy loss rates govern particle dynamics and energies. Photons are emitted along the direction of test particle motion.

¹¹ In Aristotelian electrodynamics the particle velocity is considered to be always that of the locally defined asymptotic drift trajectory.

The construction of the model γ -ray sky-maps and light curves requires a calculation of the photon phases, which should be consistent with the phases of the X-ray photons. As mentioned above, the *RV*, *MV*, and *RF* model parameters determine the orientation of the stellar field at the times corresponding to phase zero of the X-ray light curve. Following the formulation introduced in (Kalapotharakos et al. 2014), the phase of a γ -ray photon that is emitted by a particle that lies at point A reads

$$\varphi_c = \left(\Omega t_A - \phi_{v_A} - \frac{\mathbf{r}_A \cdot \mathbf{v}_A}{v_A} \frac{1}{R_{LC}} \right) \bmod 2\pi \quad (4)$$

where t_A is the integration time corresponding to the point A (assuming that the integration starts at r_{tr}), $\mathbf{v}_A, \mathbf{r}_A$ are the particle velocity and position vectors at A, and ϕ_{v_A} is the azimuth angle of the velocity \mathbf{v}_A with respect to the x axis oriented according to Ω (see Fig. 8). We note that the observer is located at $(r, \theta, \phi) = (r_{obs}, \zeta, 0)$.

The radio ephemeris defines phase zero for both γ -ray and X-ray observed light curves. We align our model X-ray light curve with the observed X-ray light curve with phase zero as defined by the radio phase zero (as in Abdo et al. 2009b; Bilous et al. 2019). The phase of our model γ -ray light curves are then computed from the orientation of the field that produced the model X-ray light curve.

The phase φ_c is measured relative to a fiducial photon that is emitted at the center of the star along the line-of-sight direction. The emission of this fictitious photon occurs at the time the observer receives the zero phase X-ray photons in the image plane from GIKS. Thus, the synchronization of the X-ray and γ -ray photons requires a modification of φ_c that takes into account the travel time from the center of the star to the observer plane. This significant nuance must be included to arrive at the correct X-ray-to- γ -ray model phasing. We are not aware of this nuance being accounted for properly in the literature. Importantly, this accounts for the deviation in curved spacetime for the X-ray photon trajectories in GIKS reaching the image plane, and is tantamount to an astrocentric clock correction. It is also important to note that photons in any given observed phase may be emitted at many mixed rotational phases owing to curved trajectories. Then, the phases of the synchronized γ -ray photons read

$$\varphi_{\gamma} = \left(\varphi_c + \frac{\Omega r_{obs}}{c} \right) \bmod 2\pi \quad (5)$$

where the second term formulates the light travel time delay with respect to the $\varphi_c = 0$ photons (see Fig. 8).

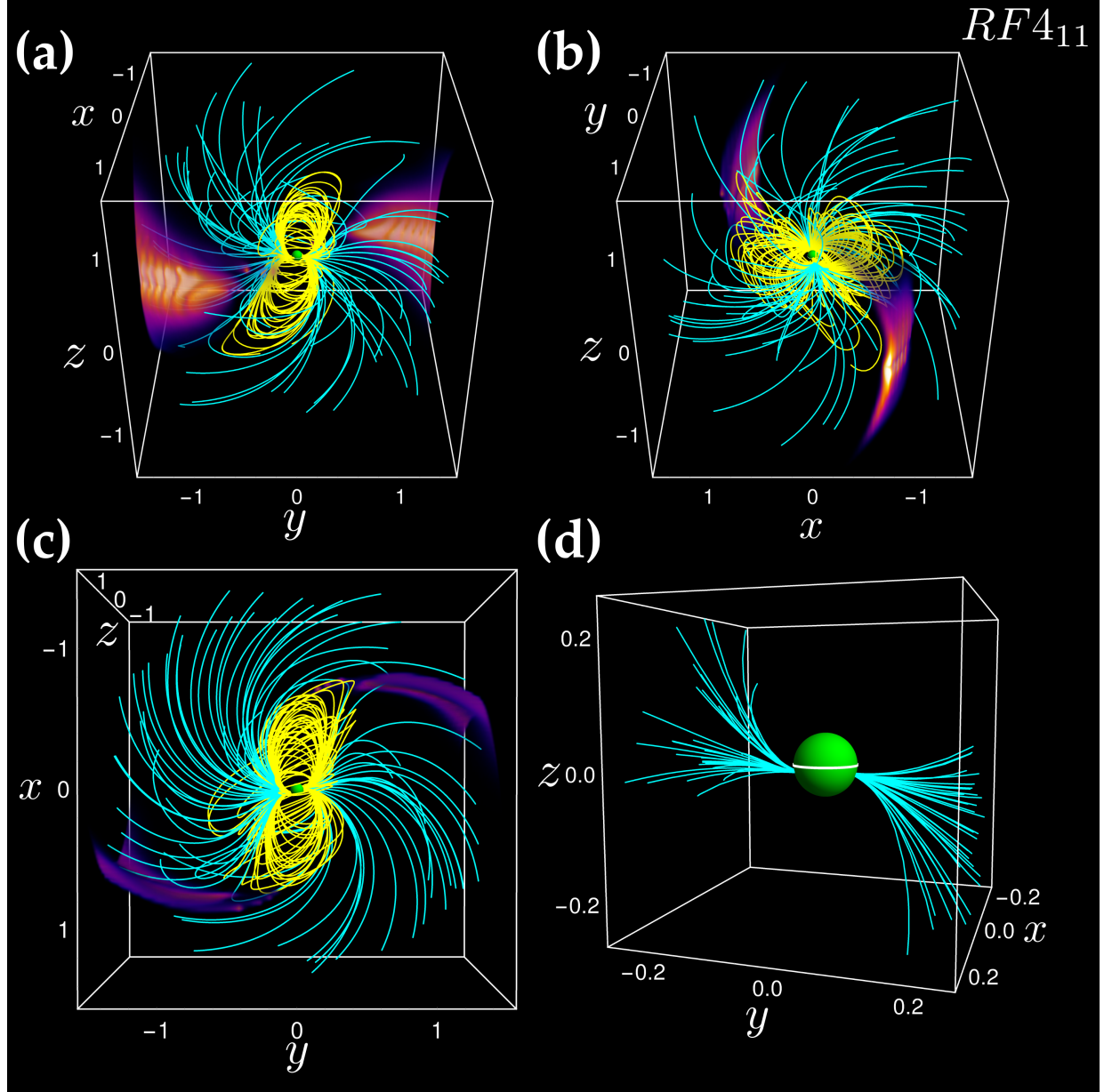


Figure 9. The field structure of the $RF4_{11}$ model. The open (closed) magnetic field lines are depicted by the cyan (yellow) colored lines. We note that the spin angular frequency vector lies along the z axis and that the unit length is normalized to $R_{LC} \approx 18r_*$. In (a)-(c), the outer magnetosphere that reaches beyond the LC is shown from different points of view. The purple-to-white colored regions in (a)-(c) denote the high values of the ratio of the accelerating electric component over the total electric field that captures the reconnection region (i.e., ECS) that emerges from the tip of the closed region. In (d), the inner magnetosphere is shown up to $5r_*$. Both polar caps (i.e., origins of the open magnetic field lines) clearly lie below the rotational equator (denoted by the white stripe).

In the right-hand column of Figs. 6–7, we plot the *Fermi-LAT* γ -ray light curve (black lines) together with the corresponding model γ -ray light curve (red lines). Recall that the *Fermi-LAT* γ -ray and *NICER* X-ray light curves are synchronized through radio ephemeris (Abdo et al. 2009b; Bilous et al. 2019) while the model γ -ray and X-ray light curves are synchronized through the phase adjustments of Eq. (5).

The model γ -ray light curves (Figs. 6–7) indicate that a field configuration that describes the observed X-ray light curve does not necessarily describe the observed γ -ray light curve. Thus, combining X-ray and γ -ray light curves could reduce the degeneracies in the possible field configurations.

The model $RF4_{11}$ does not only describe the X-ray light curve but also describes very well the peaks of

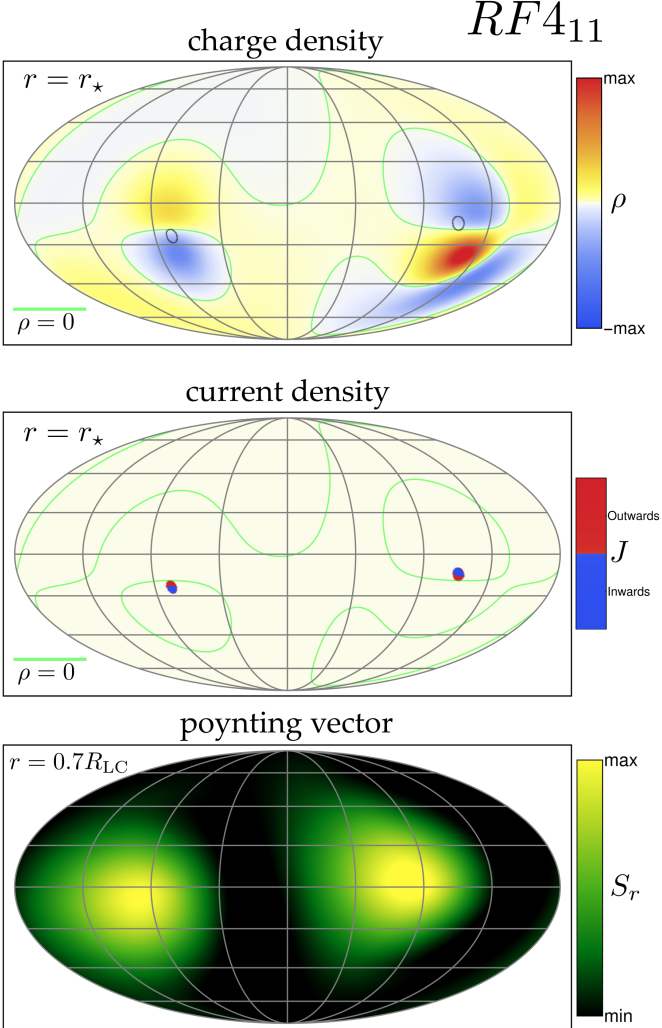


Figure 10. **Top panel:** The charge density on the stellar surface in the indicated color scale, for the $RF4_{11}$ model. The green line denotes the zero-charge line. **Middle panel:** The current density on the stellar surface. The current flows from/to the hot-spots (i.e., polar caps). The green line denotes the zero-charge line. **Bottom panel:** The strength of the radial component, S_r , of the Poynting vector on a sphere at $r = 0.7R_{LC}$.

the γ -ray light curve. The γ -ray light curves in models $RF1_{11}$ and $RF3_{11}$ seem to have the correct peak separation but the peak phases are quite off. On the other hand, the model $RF6_6$ captures well the peak phases of the γ -rays even though the peak ratio $P2/P1$ is considerably larger than the observed one. The disadvantage of this model is the rather poor statistics of the X-ray fit.

On the one hand, the generally low χ^2_r values (i.e., < 1) imply that the number of adopted parameters might be higher than what is needed for the fitting of the bolometric X-ray light curve. On the other hand, the high

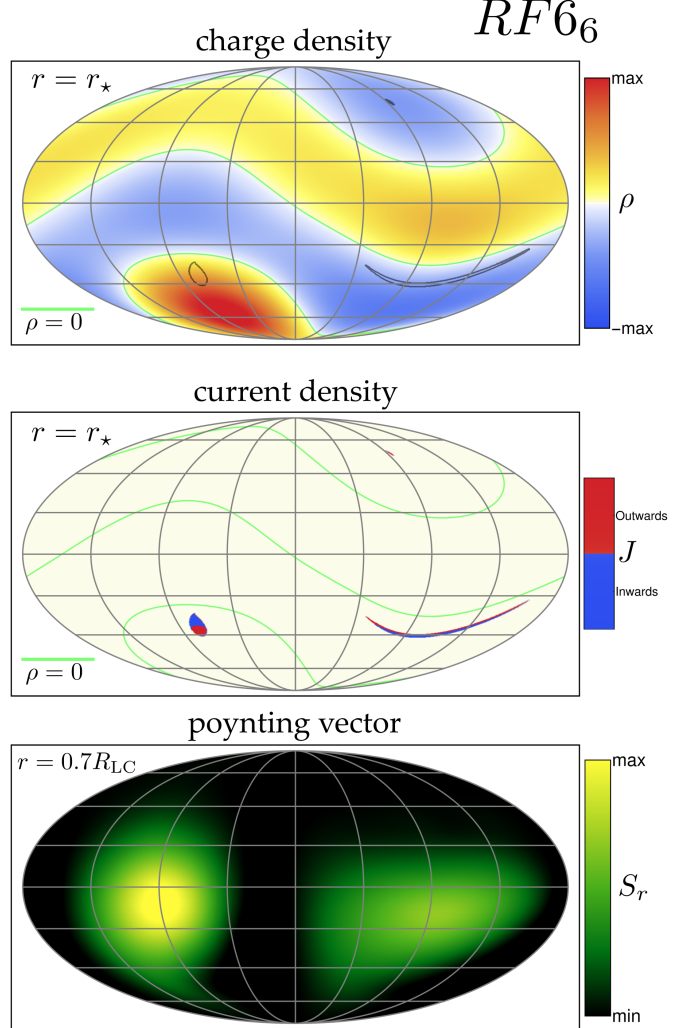


Figure 11. Similar to Fig. 10, but for the $RF6_6$ model. In this case, the two hot-spots lie in different charge polarities. The Poynting flux is asymmetric contributing to the rocket effect, which due to the rotation smoothing has mainly a component along the Ω axis.

χ^2_r value of the $RF6_6$ model as well as the performance of the model γ -ray light curves suggest that the eleven adopted parameters might be necessary for the description of the fields that fit both the *NICER* X-ray and *Fermi-LAT* γ -ray light curves.

In Fig. 9, we present the field structure of the $RF4_{11}$ model. The cyan colored lines indicate the open magnetic field lines while the yellow colored lines the closed ones. In panels (a)-(c), the outer magnetosphere (up to and beyond the LC) is shown. In these panels, the high accelerating regions (i.e., colored 3D regions) where magnetic reconnection takes place (i.e., ECS region) and most of the γ -ray emission is produced are also plotted. Panel (d) shows the inner magnetosphere up to $5r_*$. For clarity only the open magnetic field lines are

plotted. These lines originate from the corresponding two polar caps (i.e., hot-spots), which both are located in the southern rotational hemisphere, i.e., below the rotational equator which is indicated by the white stripe.

4. CONCLUSIONS

In this study, we explored SVF and FF field structures that fit the thermal X-ray light curve observed by *NICER* and *Fermi-LAT* γ -ray light curve of PSR J0030+0451.

The adopted magnetic field model consists of the sum of an offset dipole moment and an offset quadrupole $m = 0$ moment and is fully described by eleven parameters. In our modeling, the stellar mass, radius, and observer angle were fixed according to M19 and R19. Moreover, the same hot-spot temperature was adopted in agreement with the findings of M19 and R19.

Our results revealed a variety of families of SVF structures that produce hot-spots (i.e., polar caps) that superbly describe (i.e., $\chi^2_r \lesssim 1$) the bolometric X-ray light curve. The rather fast calculations of the analytic SVF models allowed a detailed MCMC exploration of the multimodal landscape corresponding to the various hot-spot families. Our analysis indicated the existence of configuration degeneracies not only between the different families but also among the same families.

We also explored SVF models with additional constraints on the field configuration that reduces the dimensionality of the parameter space. Thus, we found models that have the dipole moment at the NS center (i.e., no offset) and models where the quadrupole moment was additionally restricted to lie along the Ω (i.e., z) axis.

Starting from SVF solutions, we explored the parameter space of FF field structures that describe the X-ray light curves. However, the parameter space exploration in FF models was not as detailed as in the SVF regime due to the extremely high computational demands. Nonetheless, we found FF solutions that represent model families similar to the SVF ones. For the vast majority of the FF models the χ^2_r values were of the order of unity.

Using the realistic FF field structures that describe the X-ray light curve, we calculated synchronous γ -ray light curves and compared them to those observed by *Fermi-LAT*. For the calculation of the γ -ray light curves, we implemented the original FIDO models (Kalapotharakos et al. 2014; see also Brambilla et al. 2015; Kalapotharakos et al. 2017) that set the γ -ray emission near the ECS beyond the LC. The particle emission is due to CR and therefore, it depends on the dissipative electric fields the particles encounter and the

geometric properties (i.e., radius of curvature) of the particle trajectories.

An important nuance not reported elsewhere is the proper synchronization of model surface X-rays and magnetospheric γ -rays, which is necessary for a correct relative description of the X-ray and γ -ray light curves.

The comparison of the model γ -ray light curves with the observed one sets more constraints and potentially breaks the field degeneracies, revealing the field structure that simultaneously describes both the X-ray and γ -ray light curves. Our results identified one FF field structure that describes the X-ray light curve well and provides an adequate model of the main peaks of the corresponding γ -ray light curve. Our results also identified another FF field structure with fewer free parameters, which, even though it matches the γ -ray peak phases well, has a rather poor statistical fit of the X-ray light curve.

5. DISCUSSION

The spin-down properties of J0030+0451 suggest a surface dipole field of $B_D \sim 2 - 4 \times 10^8$ G. The radiation transport in the atmosphere starts being influenced by the magnetic field for $B_\star \gtrsim B_0 = 2 \times 10^9$ G $\approx \alpha_f^2 B_{\text{cr}}$, where α_f is the fine constant and $B_{\text{cr}} \approx 4.4 \times 10^{13}$ G is the critical field. Such influences impart anisotropy and depend on the local direction of the magnetic field. Nonetheless, the magnetic atmosphere models start becoming essential for the description of anisotropies in radiative transport of thermal emission only for $B_\star \gtrsim B_1 \approx 2 \times 10^{10}$ G (Lai 2001; Potekhin et al. 2014, W. Ho, private comm). For the vast majority of models that do consistently sample regions of $B_\star \gtrsim B_D$ across the hot spot(s) (see Figs. 2–5), the field does not exceed $\sim 10B_D \sim B_0$, which is much less than B_1 . Therefore, magnetic influences on radiation transport in these models are likely small in the *NICER* band. Our results indicate only one model (i.e., *RV5₈*) with $B_{\star\text{max}} \approx 400B_D$ that well exceeds the B_1 scale. However, even in the *RV5₈* model the hot-spot area, where the B -field reaches high values, is small and thus, likely does not substantially influence the X-ray light curve. Moreover, the actual B_D value, assuming dipole plus quadrupole field components, that is required to produce the observed spin-down power would be smaller than the nominal B_D field mentioned above (i.e., $\sim 2 - 4 \times 10^8$ G), which assumes only a pure centered dipole (see Pétri 2020). Especially for the *RV5₈* model, $B_Q/B_D = 8.68$ and therefore, the quadrupole component at the LC remains rather strong (i.e., only $\sim 0.5 \approx 8.68/18$ times smaller than the corresponding dipole one), which implies that the required B_D value would be even smaller than the nominal pure centered

dipole one. Thus, the non-magnetic atmosphere treatments in M19, R19 as well as in this study are likely secure. Finally, we note that the *NICER* band that was used in Bogdanov et al. (2019b) (i.e., $\epsilon : 0.25 - 1.45$ keV), M19 (i.e., $\epsilon : 0.4 - 3$ keV), and R19 (i.e., $\epsilon : 0.25 - 3$ keV) would sample the electron cyclotron resonance for a magnetic field $B_{\text{cr}}(\epsilon/m_e c^2) \approx 2 \times 10^{10} - 2 \times 10^{11}$ G, where m_e the electron mass and c the speed of light. These values are exceeded only for the *RV5₈* model. Nonetheless, the corresponding B_* is quite non-uniform across the polar caps and therefore, a cyclotron resonance spectral feature would be smeared for this reason, in addition to thermal and Doppler broadening.

We note that the various SVF and FF models have been derived from the maximization of the likelihood of the model X-ray light curve. An F-test would easily compare the various models both those that have the same number of parameters and those with different number of parameters. However, it is doubtful how useful this information would be with respect to the evaluation of the models on a practical level. The vast majority of the models have $\chi^2_r \approx 1$ and therefore, the determination of a model (i.e., field structure) effectiveness should incorporate the behavior of additional features (e.g., synchronous γ -ray light curve) that are essential for the overall evaluation of the model potency. Focusing solely on the statistical performance of the X-ray light curve might be misleading. In the same manner, the χ^2_r values corresponding to the SVF models (see Table 1) appear, in general, lower than the FF ones (see Table 2), which implies a better performance of the SVF models compared to the FF ones. However, even though the statistically accepted χ^2_r values of the FF models are higher than those of the SVF models, the γ -ray light-curve description requires physically realistic charges and currents of the FF models. There is no doubt that the FF field structures are more physically accurate for describing the field structure of PSR J0030+0451.

We note that in the current study we did not explore FF field structures adopting as fixed the parameter values of M19. The MCMC parameter space exploration of the FF field structures is computationally very demanding and therefore, we decided to focus on one parameter set (i.e., R19). This approach provided a clearer picture of the underlying field degeneracies even under the same adopted fixed parameter set, while it revealed the use of γ -rays is essential in setting additional constraints. Further exploration of the parameter space assuming fixed parameters that are taken from either M19 or R19 is not expected to alter the principal conclusions of this work.

A proper study of the magnetic field structure requires the incorporation of all the parameters beyond

the field-related ones. Thus, an extended free parameter space would also include M_* , r_* , ζ , hot-spot temperatures, and source distance. Increasing the number of free parameters could increase the number of field structures that adequately fit the *NICER* X-ray light curve. However, the incorporation of the X-ray photon energy dependencies may provide additional constraints. Our study makes evident that the model evaluation should include the behavior of the corresponding γ -ray light curve. Ultimately, the adopted likelihood should appropriately combine measurements of the performance of both the X-ray and the γ -ray light curves. Even though this task is computationally cumbersome, it is feasible in the near future with the tools we have developed. However, since the statistical uncertainties on the X-ray light curve are much smaller than those on the γ -ray light curve, the X-ray light curve would dominate in such a joint fit. This problem has been studied in joint fits of γ -ray and radio pulsar light curves, and requires careful treatment (Johnson et al. 2014, Seyffert et al. 2020, in prep.).

In our study, the hot-spot regions in FF magnetospheres are considered to coincide with the entire polar-cap regions. However, the polar-cap regions in FF field structures support a variety of current density distributions. The integrated total current is zero and therefore, a part of the polar cap is the origin of the direct current while the rest of the polar cap is the origin of the return current. The current patterns in the pure central dipole depend solely on the magnetic obliquity, α . The current and charge patterns across the polar caps are critical elements needed to ultimately determine the surface heating and temperature distribution. However, the polar-cap heating patterns require detailed modeling of the particles that return to the surface from the pair cascades, which is a small subset of the outflowing particles, and the heating of the atmosphere by the returning particles (Bauböck et al. 2019; Salmi et al. 2020). Therefore, the polar-cap temperature distributions cannot be estimated directly from the current and charge patterns, other than to note that regions of space-like ($J/\rho c > 1$) and return ($J/\rho c < 0$) currents enable pair cascades that will heat the polar caps but regions of time-like current ($0 < J/\rho c < 1$) will not have pair-cascades (Timokhin & Arons 2013)¹². This implies that a more accurate treatment should consider different temperatures for the re-

¹² Even though pair cascades are not activated near the stellar surface above the time-like current regions, it is still unknown whether pairs that originate from the outer magnetosphere and especially from the regions where the time-like current flows cross the zero charge surface return to the polar cap.

gions of these different current components within the same polar cap.

In the top and middle panels of Fig. 10, we plot, in the indicated color scales, the charge and current patterns, respectively on the projected stellar surface for the $RF4_{11}$ model. In this case, both polar caps are located within the negatively charged magnetosphere regions. However, in these field configurations, the zero charge line can pass through the polar caps or the polar caps can lie in different charge polarities. Figure 11 shows similarly (to Fig. 10) the charge and current density patterns for the $RF6_6$ models. In this case, the two hot-spots (i.e., polar caps) are located in regions of opposite charge polarities and therefore, in one polar cap the return current (i.e., $J/\rho c < 0$) corresponds to the inward current while in the other polar cap to the outward current.

The determination of the magnetic field structure through the thermal X-ray and γ -ray light-curve constraints and the possible field degeneracies would provide not only a deeper understanding of the corresponding emission processes but also confidence regarding the validity of the current emission modeling.

However, the implications of this study are much broader. Our modeling informs on the internal field of the MSP, albeit as an external boundary condition. How might the multipolar field configurations arise? One possibility is through the migration of the neutron and proton superfluid vortices as detailed in Ruderman (1991a,b); Chen & Ruderman (1993). Interestingly, such a migration should produce large values for z_D , and rather small values for x_D , y_D , in contrast to our model solutions. Such field migration also requires a small critical strain of the crust, in contrast to large one suggested by recent simulations (Horowitz & Kadau 2009). Another possibility is burial of the field (e.g., Payne & Melatos 2004) during the recycling process, but it is not clear that a burial mechanism is effective for permanent field reduction in MSPs or that multipolar external fields would necessarily result. Finally, we note that other unknown internal field processes, analogous to those advanced for young pulsars (e.g., Geppert & Viganò 2014; Gourgouliatos & Hollerbach 2018), but operating on much longer timescales might result in such multipolar fields.

The field structure on the stellar surface may considerably affect the efficiency of the pair production that takes place above the polar caps near the stellar surface (Timokhin & Harding 2015). For instance, higher pair multiplicity could have important implications for the locally measured energetic positrons excess (Venter

et al. 2015) or the efficiency of the pulsed γ -ray emission (Kalapotharakos et al. 2018).

The determination of the absolute phase offset of the model X-ray and γ -ray light curves in a particular magnetic field solution will also produce strong constraints on the altitude of the radio emission, since we know that the thermal X-rays are radiated at the NS surface. Radio emission heights have traditionally been estimated assuming a centered dipole field and some geometric model for the radio beam (Dyks et al. 2004). Our determination of the field structure near the NS together with the absolute phase positions of both X-ray, γ -ray and radio peaks will provide the altitude of the radio emission for a given radio beam geometry, thus constraining radio emission modeling.

Moreover, the complicated field structure would provide insight into the mechanisms for field evolution in MSPs (Viganò et al. 2013). Finally, the asymmetric fields that seem to be present at least in MSPs would contribute to the rocket effect (Harrison & Tademaru 1975; Pétri 2020). Such acceleration could be an unmodeled systematic in using MSPs to map the galactic potential. In the bottom panels of Figs. 10–11, we plot the Poynting flux, in the indicated color scale, for the $RF4_{11}$ and $RF6_6$ models, respectively on the Mollweide projection of the sphere $r = 0.7R_{LC}$. The asymmetric radiation pattern (more pronounced in $RF6_6$) will accelerate the star towards the opposite direction. However, we note that only the asymmetric component along Ω will contribute to the net-linear acceleration of the star since all the other components will be, on average, canceled out due to the fast rotation.

ACKNOWLEDGMENTS

We thank an anonymous referee for the constructive comments that helped us improving the clarity of the paper. We acknowledge helpful discussions with Wynn Ho, Slavko Bogdanov, and Zaven Arzoumanian. We especially thank Anna Watts, Thomas Riley, Anna Bilous, Cole Miller, and Fred Lamb for carefully reading and providing helpful feedback on an earlier version of this manuscript. We would also like to thank the International Space Science Institute (ISSI) for providing financial support and for the organization of the meeting of the ISSI Team that was led by I. Contopoulos and D. Kazanas. Z.W. is supported by the NASA postdoctoral program. A.K.H. and D.K are supported by the *Fermi* Guest Investigator program. This work has made use of the NASA Astrophysics Data System.

REFERENCES

- Abdo, A. A., Ackermann, M., Atwood, W. B., et al. 2009a, ApJ, 699, 1171, doi: [10.1088/0004-637X/699/2/1171](https://doi.org/10.1088/0004-637X/699/2/1171)
- . 2009b, ApJ, 699, 1171, doi: [10.1088/0004-637X/699/2/1171](https://doi.org/10.1088/0004-637X/699/2/1171) 1, 3.3.2, 3.3.2
- Bai, X.-N., & Spitkovsky, A. 2010, ApJ, 715, 1282, doi: [10.1088/0004-637X/715/2/1282](https://doi.org/10.1088/0004-637X/715/2/1282) 1
- Bauböck, M., Berti, E., Psaltis, D., & Özel, F. 2013, ApJ, 777, 68, doi: [10.1088/0004-637X/777/1/68](https://doi.org/10.1088/0004-637X/777/1/68) 3
- Bauböck, M., Psaltis, D., & Özel, F. 2019, ApJ, 872, 162, doi: [10.3847/1538-4357/aafe08](https://doi.org/10.3847/1538-4357/aafe08) 5
- Bauböck, M., Psaltis, D., Özel, F., & Johannsen, T. 2012, ApJ, 753, 175, doi: [10.1088/0004-637X/753/2/175](https://doi.org/10.1088/0004-637X/753/2/175) 2.1
- Bilous, A. V., Watts, A. L., Harding, A. K., et al. 2019, ApJL, 887, L23, doi: [10.3847/2041-8213/ab53e7](https://doi.org/10.3847/2041-8213/ab53e7) 1, 3.3.2, 3.3.2
- Bogdanov, S., Lamb, F. K., Mahmoodifar, S., et al. 2019a, ApJL, 887, L26, doi: [10.3847/2041-8213/ab5968](https://doi.org/10.3847/2041-8213/ab5968) 2.1
- Bogdanov, S., Guillot, S., Ray, P. S., et al. 2019b, ApJL, 887, L25, doi: [10.3847/2041-8213/ab53eb](https://doi.org/10.3847/2041-8213/ab53eb) 2.2, 5
- Brambilla, G., Kalapotharakos, C., Harding, A. K., & Kazanas, D. 2015, ApJ, 804, 84, doi: [10.1088/0004-637X/804/2/84](https://doi.org/10.1088/0004-637X/804/2/84) 3.3.2, 4
- Cerutti, B., Philippov, A. A., & Spitkovsky, A. 2016, MNRAS, 457, 2401, doi: [10.1093/mnras/stw124](https://doi.org/10.1093/mnras/stw124) 1
- Chen, A. Y., Yuan, Y., & Vasilopoulos, G. 2020, ApJL, 893, L38, doi: [10.3847/2041-8213/ab85c5](https://doi.org/10.3847/2041-8213/ab85c5) 1
- Chen, K., & Ruderman, M. 1993, ApJ, 408, 179, doi: [10.1086/172578](https://doi.org/10.1086/172578) 5
- Contopoulos, I., & Kalapotharakos, C. 2010, MNRAS, 404, 767, doi: [10.1111/j.1365-2966.2010.16338.x](https://doi.org/10.1111/j.1365-2966.2010.16338.x) 1
- Contopoulos, I., Kazanas, D., & Fendt, C. 1999, ApJ, 511, 351, doi: [10.1086/306652](https://doi.org/10.1086/306652) 1
- Dyks, J., Rudak, B., & Harding, A. K. 2004, ApJ, 607, 939, doi: [10.1086/383587](https://doi.org/10.1086/383587) 5
- Gendreau, K. C., Arzoumanian, Z., Adkins, P. W., et al. 2016, Society of Photo-Optical Instrumentation Engineers (SPIE) Conference Series, Vol. 9905, The Neutron star Interior Composition Explorer (NICER): design and development, 99051H, doi: [10.1111/12.2231304](https://doi.org/10.1111/12.2231304) 1
- Geppert, U., & Viganò, D. 2014, MNRAS, 444, 3198, doi: [10.1093/mnras/stu1675](https://doi.org/10.1093/mnras/stu1675) 5
- Gonthier, P. L., & Harding, A. K. 1994, ApJ, 425, 767, doi: [10.1086/174020](https://doi.org/10.1086/174020) 8
- Goodman, J., & Weare, J. 2010, Communications in Applied Mathematics and Computational Science, 5, 65, doi: [10.2140/camcos.2010.5.65](https://doi.org/10.2140/camcos.2010.5.65) 7
- Gourgouliatos, K. N., & Hollerbach, R. 2018, ApJ, 852, 21, doi: [10.3847/1538-4357/aa9d93](https://doi.org/10.3847/1538-4357/aa9d93) 5
- Gralla, S. E., Lupsasca, A., & Philippov, A. 2017, ApJ, 851, 137, doi: [10.3847/1538-4357/aa978d](https://doi.org/10.3847/1538-4357/aa978d) 1
- Gruzinov, A. 2012, arXiv e-prints. <https://arxiv.org/abs/1205.3367> 3.3.2
- Harding, A. K., & Muslimov, A. G. 2001, ApJ, 556, 987, doi: [10.1086/321589](https://doi.org/10.1086/321589) 1
- Harrison, E. R., & Tademaru, E. 1975, ApJ, 201, 447, doi: [10.1086/153907](https://doi.org/10.1086/153907) 5
- Horowitz, C. J., & Kadau, K. 2009, PhRvL, 102, 191102, doi: [10.1103/PhysRevLett.102.191102](https://doi.org/10.1103/PhysRevLett.102.191102) 5
- Jacobson, T. 2015, PhRvD, 92, 025029, doi: [10.1103/PhysRevD.92.025029](https://doi.org/10.1103/PhysRevD.92.025029) 3.3.2
- Johannsen, T., & Psaltis, D. 2010, ApJ, 718, 446, doi: [10.1088/0004-637X/718/1/446](https://doi.org/10.1088/0004-637X/718/1/446) 2.1
- Johnson, T. J., Venter, C., Harding, A. K., et al. 2014, ApJS, 213, 6, doi: [10.1088/0067-0049/213/1/6](https://doi.org/10.1088/0067-0049/213/1/6) 5
- Kalapotharakos, C., Brambilla, G., Timokhin, A., Harding, A. K., & Kazanas, D. 2018, ApJ, 857, 44, doi: [10.3847/1538-4357/aab550](https://doi.org/10.3847/1538-4357/aab550) 1, 5
- Kalapotharakos, C., & Contopoulos, I. 2009, A&A, 496, 495, doi: [10.1051/0004-6361:200810281](https://doi.org/10.1051/0004-6361:200810281) 1
- Kalapotharakos, C., Harding, A. K., & Kazanas, D. 2014, ApJ, 793, 97, doi: [10.1088/0004-637X/793/2/97](https://doi.org/10.1088/0004-637X/793/2/97) (document), 1, 3.3.1, 3.3.2, 3.3.2, 3.3.2, 4
- Kalapotharakos, C., Harding, A. K., Kazanas, D., & Brambilla, G. 2017, ApJ, 842, 80, doi: [10.3847/1538-4357/aa713a](https://doi.org/10.3847/1538-4357/aa713a) 3.3.2, 3.3.2, 4
- Kalapotharakos, C., Harding, A. K., Kazanas, D., & Wadiasingh, Z. 2019, ApJL, 883, L4, doi: [10.3847/2041-8213/ab3e0a](https://doi.org/10.3847/2041-8213/ab3e0a) 1
- Kalapotharakos, C., Kazanas, D., Harding, A., & Contopoulos, I. 2012, ApJ, 749, 2, doi: [10.1088/0004-637X/749/1/2](https://doi.org/10.1088/0004-637X/749/1/2) 3.3.1
- Kelner, S. R., Prosekin, A. Y., & Aharonian, F. A. 2015, AJ, 149, 33, doi: [10.1088/0004-6256/149/1/33](https://doi.org/10.1088/0004-6256/149/1/33) 3.3.2
- Lai, D. 2001, Reviews of Modern Physics, 73, 629, doi: [10.1103/RevModPhys.73.629](https://doi.org/10.1103/RevModPhys.73.629) 5
- Lo, K. H., Miller, M. C., Bhattacharyya, S., & Lamb, F. K. 2013, ApJ, 776, 19, doi: [10.1088/0004-637X/776/1/19](https://doi.org/10.1088/0004-637X/776/1/19) 1
- Miller, M. C., & Lamb, F. K. 2015, ApJ, 808, 31, doi: [10.1088/0004-637X/808/1/31](https://doi.org/10.1088/0004-637X/808/1/31) 1
- Miller, M. C., Lamb, F. K., Dittmann, A. J., et al. 2019, ApJL, 887, L24, doi: [10.3847/2041-8213/ab50c5](https://doi.org/10.3847/2041-8213/ab50c5) (document), 1, 2.1, 5, 1, 2.2, 3.1, 4, 3.2, 4, 5
- Payne, D. J. B., & Melatos, A. 2004, MNRAS, 351, 569, doi: [10.1111/j.1365-2966.2004.07798.x](https://doi.org/10.1111/j.1365-2966.2004.07798.x) 5
- Pétri, J. 2015, MNRAS, 450, 714, doi: [10.1093/mnras/stv598](https://doi.org/10.1093/mnras/stv598) 1

- . 2016, MNRAS, 463, 1240, doi: [10.1093/mnras/stw2050](https://doi.org/10.1093/mnras/stw2050)
- . 2020, MNRAS, doi: [10.1093/mnras/staa3086](https://doi.org/10.1093/mnras/staa3086) 5
- Philippov, A. A., & Spitkovsky, A. 2018, ApJ, 855, 94, doi: [10.3847/1538-4357/aaabbc](https://doi.org/10.3847/1538-4357/aaabbc) 1
- Ploeg, H., Gordon, C., Crocker, R., & Macias, O. 2020, arXiv e-prints, arXiv:2008.10821, <https://arxiv.org/abs/2008.10821> 1
- Potekhin, A. Y., Chabrier, G., & Ho, W. C. G. 2014, A&A, 572, A69, doi: [10.1051/0004-6361/201424619](https://doi.org/10.1051/0004-6361/201424619) 5
- Psaltis, D., & Johannsen, T. 2012, ApJ, 745, 1, doi: [10.1088/0004-637X/745/1/1](https://doi.org/10.1088/0004-637X/745/1/1) 2.1
- Psaltis, D., & Özel, F. 2014, ApJ, 792, 87, doi: [10.1088/0004-637X/792/2/87](https://doi.org/10.1088/0004-637X/792/2/87) 2.1
- Riley, T. E., Watts, A. L., Bogdanov, S., et al. 2019, ApJL, 887, L21, doi: [10.3847/2041-8213/ab481c](https://doi.org/10.3847/2041-8213/ab481c) (document), 1, 2.1, 1, 2.2, 3.1, 2, 4, 3.2, 4, 5
- Ruderman, M. 1991a, ApJ, 366, 261, doi: [10.1086/169558](https://doi.org/10.1086/169558) 5
- Ruderman, R. 1991b, ApJ, 382, 576, doi: [10.1086/170744](https://doi.org/10.1086/170744) 5
- Salmi, T., Suleimanov, V. F., Nätilä, J., & Poutanen, J. 2020, A&A, 641, A15, doi: [10.1051/0004-6361/202037824](https://doi.org/10.1051/0004-6361/202037824) 5
- Spitkovsky, A. 2006, ApJL, 648, L51, doi: [10.1086/507518](https://doi.org/10.1086/507518) 1
- Timokhin, A. N. 2006, MNRAS, 368, 1055, doi: [10.1111/j.1365-2966.2006.10192.x](https://doi.org/10.1111/j.1365-2966.2006.10192.x) 1
- Timokhin, A. N., & Arons, J. 2013, MNRAS, 429, 20, doi: [10.1093/mnras/sts298](https://doi.org/10.1093/mnras/sts298) 5
- Timokhin, A. N., & Harding, A. K. 2015, ApJ, 810, 144, doi: [10.1088/0004-637X/810/2/144](https://doi.org/10.1088/0004-637X/810/2/144) 5
- Venter, C., Kopp, A., Harding, A. K., Gonthier, P. L., & Büsching, I. 2015, ApJ, 807, 130, doi: [10.1088/0004-637X/807/2/130](https://doi.org/10.1088/0004-637X/807/2/130) 5
- Viganò, D., Rea, N., Pons, J. A., et al. 2013, MNRAS, 434, 123, doi: [10.1093/mnras/stt1008](https://doi.org/10.1093/mnras/stt1008) 5
- Wasserman, I., & Shapiro, S. L. 1983, ApJ, 265, 1036, doi: [10.1086/160745](https://doi.org/10.1086/160745) 8